Structural Isomer of Fluorinated Ruddlesden-Popper Perovskites Toward Efficient and Stable 2D/3D Perovskite Solar Cells

Junseop Byeon, Seong Ho Cho, Junke Jiang, Jihun Jang, Claudine Katan, Jacky Even, Jun Xi, Mansoo Choi, Yun Seog Lee

Structural isomer of fluorinated Ruddlesden-Popper perovskite towards efficient and stable 2D/3D perovskite solar cells

Junseop Byeon[1,2†], Seong Ho Cho[1,6†], Junke Jiang[3], Jihun Jang[2], Claudine Katan[3], Jacky Even[4], Jun Xi[5], Mansoo Choi[1,2]*, Yun Seog Lee[1,6]**

[1]Department of Mechanical Engineering, Seoul National University, Seoul 08826, Republic of Korea

[2]Global Frontier Center for Multiscale Energy Systems, Seoul National University, Seoul 08826, Republic of Korea

[3] University of Rennes, ENSCR, CNRS, ISCR, UMR 6226, F-35000 Rennes, France

[4] Univ Rennes, INSA Rennes, CNRS, Institut FOTON - UMR 6082, F-35000 Rennes, France

[5]Key Laboratory for Physical Electronics and Devices of the Ministry of Education & Shaanxi Key Lab of Information Photonic Technique, School of Electronic Science and Engineering, Xi'an Jiaotong University, No.28, Xianning West Road, Xi'an, 710049, China

[a]Inter-University Semiconductor Research Center, Seoul National University, Seoul 08826, Republic of Korea

* Corresponding authors

E-mail: mchoi@snu.ac.kr, jun.xi@xjtu.edu.cn, leeyunseog@snu.ac.kr

[†]J.B. and S.H.C contributed equally to this paper

Keywords: structural isomer, Ruddlesden-Popper perovskite, 2D perovskite, stability, intermolecular stacking

ToC figure

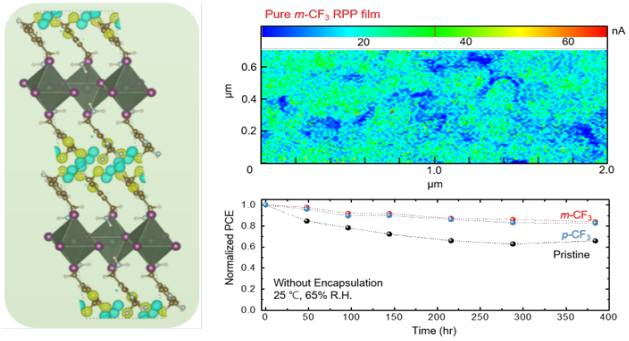

Two types of structural isomers, *meta*- and *para*-CF_3 groups linked to phenethylammonium iodide (PEAI), were systematically investigated as interface modifiers. Compared to *para*-CF_3-PEAI, the *meta*-CF_3-PEAI based perovskite is characterized by shorter interlayer distances, different surface dipoles and band alignments. The molecular substitution leads in turn to the enhancement of the vertical charge transport and to a superior suppression of non-radiative recombinations. *meta*-CF_3-PEAI as modifier on the 3D perovskite absorber results in an improvement of the power conversion efficiency to 22.4% as well as enhanced stability against humidity and light illumination.

Abstract

Defect passivation using two-dimensional (2D) layered perovskites with organic spacers on 3D bulk perovskite has been proposed as an effective strategy to improve perovskite solar cell stability and efficiency. Specifically, fluorination of the organic spacers has been employed due to the resulting hydrophobic nature and the defect passivation characteristics. In addition to the type of functional group attached to the spacer molecules, conformational changes of fluorine isomers on layered perovskite can provide an extended strategy to control a variety of opto-electrical properties related to the interlayer spacing. As a model system for the structural isomer of fluorinated spacer, *meta*-CF_3 and *para*-CF_3 groups anchored to phenethylammonium iodide (PEAI) spacer molecules are employed to synthesize 2D perovskites and to investigate their full potential as an interfacial modifier for perovskite solar cells. The fluorination position change leads to altered opto-electrical characteristics in layered perovskites. Although they possess identical functional groups, the different orientations of the functional groups used in the perovskite layer deposited on the 3D perovskite absorber, result in distinct electrical properties of the 2D/3D heterostructures due to the dissimilar intermolecular interactions. The 2D perovskite with *meta*-CF_3-PEAI spacer exhibits an enhanced the charge transport in the out-of-plane orientation and a suppression of the trap states of 3D perovskite while also providing a more favorable energy alignment for efficient charge transfers. Theoretical simulations are consistent with the experimental results. The structural isomers of fluorination anchoring to spacer cations indeed alter the structural configuration of the spacer as well as reduce inter-layer spacing that can improve the performance and the stability of 2D/3D perovskite solar cells.

Introduction

Organic-inorganic hybrid halide perovskites based solar cells (PSC) have demonstrated a power conversion efficiency (PCE) that exceeds 25% from polycrystalline thin-films due to their defect tolerance, long carrier diffusion length, high optical absorption coefficients, and tunable bandgap.[1-5] Despite the remarkable progress in PCE, there are still challenges remaining before PSCs can be commercialized, mostly related to long-term stability. In general, oxygen and humidity have been considered as the key external sources for degradation.[6-7] Even when stored in an inert atmosphere, PSCs undergo degradation under long-term light illumination condition.[8,9] Previous studies have revealed that the instability of PSC originates from trapped charges and ion migration which are relevant to the defects in the perovskite layer, such as those related to interstitial iodide and under-coordinated Pb^{2+}.[10-14] The migration of defects can easily be stimulated by excess charges, a high electric field, and light illumination, resulting in material decomposition as well as degraded device performances.[11-13,15-17] Thus, mitigating the defect-related degradation of the perovskite layer in PSC is highly desirable to improve the long-term stability.[18-20]

Quasi-two-dimensional Ruddlesden-Popper perovskites (RPP) ($(A')_2(A)_{n-1}Pb_nX_{3n+1}$, where n is the number of octahedral slab layers; A' is the spacer ligand; A denotes small cations such as $CH_3NH_3^+$, $CH(NH_2)_2^+$, and Cs^+; and X is halide anion) are emerging due to their enhanced stability against oxygen and humidity[21-24] The periodic intercalation of long spacer ligands into inorganic slabs can passivate defects as well as impede the migration of defects by separating the 3D perovskite layers. However, long spacer ligands can also reduce electrical conductivity across the 2D perovskite layers, thereby often resulting in a limited PCE when using a pure RPP layer as a light-absorber.[24-28] Instead, a bilayer configuration of 2D/3D perovskite that integrates a RPP layer in tens of nanometers thickness as an interfacial layer between a 3D perovskite layer and a hole-transporting

layer (HTL) has been successfully employed, demonstrating significant enhancements of both the performance and stability of PSCs.[29-31]

Most progress in 2D/3D perovskite solar cells thus far has been related to the engineering of the opto-electronic properties of RPPs by changing the type of spacer ligands, which typically comprise conjugated oligomers, aliphatic ammoniums, and single aromatic rings.[32] Among the many types of organic spacers, organic ligands with fluorinated functional groups have shown enhanced hydrophobicity of RPPs, further improving the stability of the 2D/3D PSCs.[33-35] In fact, the fluorinated functional molecules with ammonium terminal have been utilized to take various effects on improving the device performance. For instance of 2D/quasi-2D perovskites, fluorinated molecule, 4-fluorophenethylammonium, is found to control the phase distribution of RPP and enhance charge transport.[36-38] Furthermore, fluorinated molecule, 2,3,4,5,6-pentafluorophenethylammonium, efficiently passivates the trap states at surfaces and grain boundaries of 3D perovskite without forming 2D phases, improving thermal stability.[39] Hence, designing fluorinated functional spacers plays significant role in formation of 2D/3D structure.[39]

Several studies have proposed organic cations with multiple fluorine atoms such as trifluoromethyl (CF_3-) groups linked to an aromatic ring.[40] 2-CF_3-PEAI (2-trifluoromethyl-phenylethylamine hydroiodide) can be used as a trap deactivator for perovskite solar cells, improving performance and stability[41]. In addition to the category of functional group, the position of the functional group is also found to be crucial because fluorination with different positions in the aromatic ring affects the distribution of electron clouds, which can change the dipole moment and affect the crystal structure of the 2D perovskite layers.[37,43,44] Moreover, previous studies reported that the stacking and orientational modes of the crystal are influenced by the fluorination position, even with the same chemical formula, resulting in different abilities of the defect passivation and

charge transport properties.[35,38] Therefore, understanding how the isomer structure affects the opto-electronic characteristics of the RPP interface layer can provide a pathway by which to realize the full potential of the RPP interface layer for highly efficient and stable PSCs.

Herein, we systematically investigate the effects of novel steric fluorine-rich groups on the organic ligands of phenethylammonium (PEA) and the assembly of their mono-layered (n = 1) RPPs as interface layers on 3D perovskite to enhance device performance and stability levels. 2D phase-pure (n = 1) RPPs with different fluorinated CF_3-PEA cations, 2-(3-trifluoromethylphenyl)ethanamine and 2-(4-(trifluoromethyl)phenyl)ethanamine, are prepared. Interestingly, despite the similar inorganic framework, two similar RPPs possess different opto-electronic properties and dissimilar intermolecular stacking modes between the adjacent organic cations. Specifically, the 2-(3-trifluoromethylphenyl)ethanamine based 2D structure (n = 1) exhibits enhanced inter-layer hybridization, larger dipole moment, and enhanced out-of-plane conductivity. Accordingly, the out-of-plane charge transport in such 2D structure (n = 1) can be more favorable. By forming highly oriented monolayered RPPs on 3D perovskites, the effects of a structural isomer on their crystallinity and electronic band alignments for hole transfer are investigated to understand how the fluorinated isomers affect suppression of non-radiative losses and improvement of the carrier lifetimes in PSCs. Furthermore, 2D/3D PSCs are fabricated with RPPs, demonstrating an improved PCE as well as enhanced device stability against humidity, retaining 85% of the initial PCE after 385 hours at a relative humidity of 65% without encapsulation.

Results and Discussion

As a model system for the structural isomer of fluorinated spacer, *meta*-CF_3 and *para*-CF_3 groups anchored to PEAI molecules are prepared to form PEAI-based RPPs. To synthesize fluorinated organic spacers, 2-(3-trifluoromethylphenyl)ethanamine and 2-(4-trifluoromethylphenyl)ethanamine were both dissolved in methanol. Aqueous solutions of HI were added dropwise in the precursors to induce an additional reaction with the amine functional group. **Figure 1a** shows the chemical structures of the precipitated iodide salts, in this case *meta*-CF_3 PEAI and *para*-CF_3 PEAI. Hereafter, we designate the *meta*-CF_3 PEAI and *para*-CF_3 PEAI as *m*-CF_3 and *p*-CF_3, respectively. The abbreviations *m*-CF_3 and *p*-CF_3 correspond to the locations of the trifluoromethyl (CF_3) functional groups at the *meta*- and *para*- position respective to the ethanamine terminal. Nuclear magnetic resonance (NMR) spectroscopy was conducted to examine the chemical structures of *m*-CF_3 and *p*-CF_3. As shown in **SI Figure S1**, the close ^{19}F resonances in both cases indicate identical fluoride moieties shared by these two molecules. ^{13}C resonance with split peak is observed for *m*-CF_3 compared to *p*-CF_3, verifying the molecular structure with diverse CF_3 group positions.

The synthesized *m*-CF_3 and *p*-CF_3 ligands were then used to prepare two different structural-isomer-anchored RPPs. The $n = 1$ phase RPPs were fabricated by spin-coating precursor solutions onto glass substrates and annealing them at 100 °C. Their chemical formulae are given by (*meta*-CF_3-PEA)$_2$PbI$_4$ (*m*-CF_3 RPP) and (*para*-CF_3-PEA)$_2$PbI$_4$ (*p*-CF_3 RPP), respectively. As shown in **Figure 1b**, the X-ray diffraction (XRD) spectra of both samples indicate the formation of a phase-pure RPP structure with *n* equal to 1 in the P1 space group. The lattice distances of the (002) plane are calculated and found to be 20.15 Å and 17.95 Å for the *m*-CF_3 and *p*-CF_3 RPPs, respectively. Interestingly, the *m*-CF_3 RPP exhibits a larger lattice constant along the out-of-plane orientation

than that of the *p*-CF_3 RPP. The different spacings between the layers suggest a difference in the stacking modes originated from the altered direction and the magnitude of the hydrogen bond or van der Waals interaction between the two organic spacers.[38,44,45] In addition, Cross-sectional scanning electron microscopy (SEM) images of indium-tin-oxide (ITO) / RPP / Au samples, prepared by spin-coating of precursors with equimolar concentrations of 1 M, show the formation of layered 2D plates (**SI Figure S2a**). The *m*-CF_3RPP sample has a thickness of 1.0 μm, which is thicker the *p*-CF_3 RPP sample's thickness of 0.48 μm.

The origin of the different inter-layer spacing values originated from the fluorination position on the intermolecular interactions and physical properties are investigated by density-functional theory (DFT) simulations. **SI Figure S3** shows schematics of the simulated intermolecular ordering for both single-crystalline *m*-CF_3 RPP and *p*-CF_3 RPP, describing the intercalation of bulky organic spacers into the 2D sheets of $[PbI_6]^{4-}$ octahedra. The relative binding energy between the adjacent couple *m*-CF_3 RPP layer (6.82 meV□Å^{-2}) is calculated to be lower than *p*-CF_3 RPP (10.08 meV□Å^{-2}), indicating the interlayer binding strength of *m*-CF_3 RPPs is smaller. The DFT calculation results show that the benzene rings within the *m*-CF_3 RPPs have a more favorable stacking mode.[36,46] The differences in the intermolecular stacking modes can originate from the relatively distinct interactions between multiple fluorine (F···F) groups on the terminals of the benzene moieties (**SI Figure S3**). Similar to the result from the XRD measurement, the simulated values of (002) plane lattices constant along the layer stacking direction of *m*-CF_3 (18.57 Å) is greater than that of *p*-CF_3 RPPs (17.88 Å), correlating with the estimated lattice distance result from the XRD patterns.

More importantly, the calculated charge density difference between organic and inorganic regions shows evident hybridization between *m*-CF_3, while it is negligible for *p*-CF_3 (**SI Figure**

S3b). Slightly enhanced out-of-plane conductivity of *m*-CF_3 RPP can be expected in comparison to that of the *p*-CF_3 RPP due to the favorable interlayer hybridization of the *m*-CF_3 RPPs. The band structures of *m*-CF_3 and *p*-CF_3 RPP were calculated, and the band gap values were found to be 1.61 eV and 1.56 eV, respectively (**SI Figure S4**). While the computed band gap values are smaller than the experimental values as expected from DFT calculations at the PBE level , a larger band gap for m-CF3 is is nevertheless also predicted by the calculations. The computed band gap values are sensitive to the distortions of the perovskite backbone due to the presence of the spacer molecules. Indeed, the electronic band gaps of 2D perovskites are affected by both in-plane (β) and out-of plane (δ) angular distorsions,[26] which amount to 17.9° (19.4°) and 15.3° (12.2°) respectively, for *p*-CF_3 (*m*-CF_3). There is therefore a larger in-plane but smaller out-of plane angular distorsion for *m*-CF_3 by comparison to *p*-CF_3 resulting however in a net increase of the band gap as observed experimentally.

Slab models were further constructed to study the polarization profiles along the stacking axes (**SI Figure S5**), the polarization density profiles (**SI Figure S6**) were calculated to evaluate the surface dipole density p of each 2D RPP, equal to 4.84×10^{-11} C/m and 5.19×10^{-11} C/m for *m*-CF_3 and *p*-CF_3 RPP, respectively. Using the equation $\Delta E_V^{abs} = -1.809 \times 10^{-8}\, \Delta p$,[71] the maximum of the valence band *m*-CF_3 RPP is predicted to lie 0.40 eV higher than that of *p*-CF_3 RPP. This agrees well with the experimentaltrend of the ionization energies, with a value for *m*-CF_3 layered perovskite found 0.30 eV smaller than that of *p*-CF_3 layered perovskite (5.5 eV vs. 5.8 eV). The calculated present dipole moment (1.3 D) of *m*-CF_3 localized in 2D structure is found to be higher than that (0.3 D) of *p*-CF_3 from structural formula using DFT calculations, which can facilitate the dissociation of photo-generated excitons (**SI Table S1**).[37] The larger molecular dipole of *m*-CF_3

may however lead to a smaller surface dipole, since this quantity depends on the alignment of the molecular dipole with the stacking axis perpendicular to the surface.[71]

Additionally, as shown in **SI Figure S7**, the dielectric constant of *m*-CF_3 RPP is found to be only slightly larger than that of *p*-CF_3 (4.28 vs 4.02), while the dielectric constant of sole spacers are almost the same. Therefore a large difference in exciton binding energies is not expected, consistently with experimental observations (Table 1).

The carrier transport properties of the RPPs in out-of-plane orientation were measured by using conductive atomic force microscopy (C-AFM). Both *m*-CF_3 RPP and *p*-CF_3 RPP samples were prepared by spin-coating precursor solutions of 1 M concentration on ITO-coated glass substrates to apply a voltage bias to RPPs in out-of-plane orientation between an AFM tip and the ITO layer. **Figure 1c**, **1d** and **SI Figure S8** show profiles of measured current and surface topology, respectively. Although the *m*-CF_3 RPP thin-film (1 μm) is thicker than that of *p*-CF_3 RPP (0.48 μm), the *m*-CF_3 RPP thin-film shows a significantly higher current level than *p*-CF_3 RPP under the same bias condition across the entire measurement area.

The use of different organic spacers in RPP can also affect the as-formed quantum well structure, resulting in different electronic band structures. **Figure 1e** and **1f** show spectra of the steady-state photoluminescence (PL) and UV-VIS optical absorbance spectra of *m*-CF_3 RPPs and *p*-CF_3 RPPs. The PL peaks of the *m*-CF_3 RPP and *p*-CF_3 RPP are measured to be at 2.51 and 2.30 eV, respectively. The PL peaks are highly correlated with the exciton peaks (E_{s1}) of 2.57 and 2.37 eV from the optical absorbance spectra (**SI Figure S2b**), which suggests the formation of strongly bonded excitons produced from typical quantum-well-like regimes in the RPP structures. In addition, the continuum edges of the *m*-CF_3 and *p*-CF_3 RPPs are estimated to exist at 2.83 and 2.65

eV, respectively (**Figure 1e,f, Table 1**). The exciton binding energy levels (E_b) of the *m*-CF_3 RPP and *p*-CF_3 RPP are 260 and 280 meV, respectively, as determined from the continuum edge by subtracting the exciton peak energy (**Table 1**). This difference in the E_b can also contribute to a lower recombination of photogenerated carriers in the 2D/3D stacked heterostructure, as predicted from the calculated dipole moments localized in the 2D structure.

The *m*-CF_3 RPP and *p*-CF_3 RPP are then used to fabricate PSCs with a 2D/3D configuration. Phase-pure (n = 1) RPPs with *m*-CF_3 and *p*-CF_3 as spacers are deposited on the surfaces of formamidinium (FA)-excess triple-cation 3D perovskite thin-films by a two-step spin-coating process. The *m*-CF_3 and *p*-CF_3 spacers were pre-dissolved in IPA solutions. SEM images show that the fabricated 2D/3D perovskite thin-film stacks assembled with the *m*-CF_3 and *p*-CF_3 RPPs treatment possess similar surface morphologies to those of pristine 3D perovskite thin-films (**SI Figure S9**). Grazing-incidence wide-angle X-ray scattering (GI-WAXS) measurements were carried out to identify the existence of RPP layers on 3D perovskite thin-films and their crystal orientations. Before applying the RPP layers, the 3D perovskite thin-film show broad Debye–Scherrer rings at 1.0 $Å^{-1}$ with sharp Bragg peaks at 0.9 $Å^{-1}$ along the out-of-plane direction (q_z), indicating the formation of randomly oriented 3D perovskites and a highly oriented PbI_2 (001) phase, as shown in **Figure 2a**.

After the *m*-CF_3 or *p*-CF_3 treatments on the 3D perovskite thin-film, signals from the PbI_2 phases are slightly reduced and a new pair of sharp Bragg spots along the q_z direction are emerged, which indicate the formation of the (002) and (004) planes of the phase-pure (n = 1) RPPs. The *m*-CF_3- and *p*-CF_3-treated 2D/3D perovskite thin-films show peaks at 4.4° and 4.8°, respectively, belonging to the (002) planes. Notably, azimuthal angle scans along the (002) plane show a much sharper peaks from the *m*-CF_3-treated sample than the *p*-CF_3-treated sample, suggesting highly oriented

growth of the phase-pure *m*-CF_3 RPP layer on the 3D perovskite (**Figure 2b**). The highly orientated grown *m*-CF_3 RPP with stacking mode close to face-to-face could achieve high performance PSCs by enhancing charge transport out-of-plane direction to the substrate plane.[47-49] Furthermore, out-of-plane GI-WAXS profiles show that the *m*-CF_3 treatment has a stronger effect on reducing the PbI_2 phases and enhancing the 3D phases compared to the *p*-CF_3 case, an outcome also correlated with the GI-XRD measurements (**Figure 2c** and **SI Figure S10**). The XRD measurements of the perovskite films also show a slight decrease in PbI_2 and an increase in the α-phase of the perovskites after the RPP treatments, suggesting interfacial Pb-related defect passivation (**SI Figure S11**).[10] Therefore, the *m*-CF_3 RPP not only benefits the crystallinity of the perovskite film but also facilitates the monolayered (n = 1) RPP formation in *c*-axis parallel to the substrate with high out-of-plane charge transport

The optical absorbance spectra in **Figure 3a** demonstrate that both the *m*-CF_3- and *p*-CF_3-treated perovskites show a slight blue shift absorbance onset (4–5 nm) and an increasement in the absorbance intensity in the range of 400–550 nm after the formation of RPPs upon the 3D perovskite films. The higher absorbance intensity of the *m*-CF_3-treated 2D/3D perovskite than the *p*-CF_3-reated specimen is likely due to the formed relatively thicker 2D film treated by *m*-CF_3 in an identical concentration. In addition, the photoluminescence (PL) intensity is increased after the RPP treatment. The perovskite treated with *m*-CF_3 RPP shows the strongest PL emission, suggesting more effective passivation of non-radiative recombination centers (**Figure 3b**). In addition, the blue shifts in the PL peaks of both *m*-CF_3 and *p*-CF_3 2D/3D heterostructures also suggest filled trap states at the sub-bandgaps.[50-54] This correlates with the enhanced charge carrier lifetimes of the 2D/3D heterostructures found in the time-resolved PL (TRPL) measurements (**SI**

Figure S12). Both PL measurements highlight the fact that the phase-pure (n = 1) RPPs with m-CF_3 more effectively suppress the non-radiative recombination of 3D perovskite than p-CF_3.

The defect passivation effect of 2D RPPs treatment is further examined by space-charge-limited current (SCLC) measurements to compare actual trap-state density in the 2D/3D perovskite thin-films. Electron-only types of SCLC devices are prepared with a structure of ITO / SnO_2 / stacked 2D/3D heterostructure perovskite / C_{60} / Au. As shown in **Figure 3c**, the trap-filled limit voltages (V_{TFL}) of pristine 3D perovskite, m-CF_3-treated perovskite, and p-CF_3-treated perovskite specimens are estimated to be 0.133, 0.113, and 0.121 V, respectively (**SI Table S2**). The trap density (n_t) can be calculated from the following equation:

$$V_{\mathrm{TFL}} = \frac{e n_t d^2}{2\varepsilon\varepsilon_0}$$

, where e, d, ε_0, and ε are the elementary charge, the thickness of perovskite thin-films, the vacuum permittivity, and the dielectric constant of the perovskite thin films, respectively. The estimated n_t values of the pristine 3D perovskite, the m-CF_3-based 2D/3D heterostructure, and the p-CF_3-based 2D/3D perovskites are 1.34×10^{15}, 1.02×10^{15}, and 1.17×10^{15} cm^{-3}, respectively. In addition, X-ray photoelectron spectroscopy (XPS) of the 2D/3D heterostructures shows that the both RPPs have significantly reduce metallic Pb_0 states with new fluorine moieties that form on the surfaces (**SI Figure S13**). It is reported that Pb_0 can be generated during fabrication process and act as a non-radiative recombination center. The strong electronegativity of CF_3 group could effectively eliminate metallic lead with deep level defect.[41] Consistent with previous studies, the SCLC and XPS results indicate that both CF_3 isomers with different meta- and para-positions can effectively suppress deep-level traps of Pb_0 at the perovskite interface by forming phase-pure (n = 1) RPPs.[55,56]

The band alignments of the RPPs in 2D/3D perovskites are examined by using ultraviolet photoelectron spectroscopy (UPS). The Fermi level (E_F) and the energy band alignments between the 2D and 3D perovskite layers are shown in **Figure 3d** and **SI Figure S14**. The valence band positions (E_{VB}) of the *m*-CF_3 and of the *p*-CF_3 2D phase-pure (n = 1) RPPs are measured to be 5.50 ± 0.1 and 5.80 ± 0.1 eV, respectively. Considering the bandgap of the materials, the conduction band positions (E_{CB}) of the *m*-CF_3 and *p*-CF_3 monolayered RPPs are estimated to be 3.00 ± 0.1 and 3.50 ± 0.1 eV, respectively. As depicted in **Figure 3d**, the estimated band alignment at the 2D/3D heterostructure suggests that *m*-CF_3 provides favorable band positions for hole transfers, whereas *p*-CF_3 can create a hole barrier of approximately 0.08 eV. It should be noted that the estimated band alignment show that the E_{VB} of *m*-CF_3 RPP is 0.30 eV higher than that of *p*-CF_3 RPP, which agrees well with the theoretically calculated 0.40 eV difference.

Based on the beneficial characteristics of RPPs treatment on the 3D perovskite thin films, PSCs with the 2D/3D perovskite heterostructure are fabricated. An *n-i-p* structure of ITO / SnO_2 / perovskite / Spiro-OMeTAD / Au are used. The optimal precursor concentration is determined from the current density *vs*. bias (*J-V*) measurement as shown in **SI Figure S15**. The PSCs with a precursor concentration of 3 mg□ml^{-1} exhibit the highest PCE. The decrease in PCE at higher concentrations is possibly due to the formation of excessively thick RPP layers or unreacted 2D salts remaining at the interfaces.[57,58] Cross-sectional SEM images of the devices show the formation of ultrathin RPP layers on the 3D perovskite layers (**SI Figure S16**). As shown in **Figure 4**, **SI Figure S17**, and **S18**, statistical histograms of the device performances after the *m*-CF_3 and *p*-CF_3 treatments with anti-reflective films reveal increases in the average short-circuit current density (J_{SC}) to 24.2 and 23.9 mA·cm^{-2}, respectively. The highest J_{SC} from the *m*-CF_3 RPP treatment suggests efficient hole transfers caused by the favorable band alignment and the enhanced out-of-plane

conductivity by the face-to-face stacking mode. Moreover, while the pristine PSCs exhibit an average open-circuit voltage (V_{oc}) of 1.13 V, the *m*-CF_3 RPP and *p*-CF_3 RPP treated PSCs show V_{oc}s of 1.17 and 1.16 V, respectively. The corresponding V_{oc} deficits (($E_g \square q^{-1}$) – V_{oc}) are calculated to be 0.432, 0.402, and 0.403 V for pristine, *m*-CF_3-treated, and *p*-CF_3-treated PSCs, respectively.[54-56] The PSCs of the champion devices realized by the *m*-CF_3 and *p*-CF_3 RPP treatments are 22.4% and 21.3%, respectively, showing significant improvements compared to the PCE of the pristine device of 20.9%. The stabilized power output (SPO) of the *m*-CF_3-treated perovskite was 21.9% at a maximum power point bias of 0.968 V, showing a similar PCE from the *J-V* curves (**SI Figure S19**). In addition, flexible devices were also fabricated using ITO / PEN film, demonstrating PCEs of 17.7%, 18.6%, and 18.4% for pristine, *m*-CF_3-treated, and *p*-CF_3-treated flexible PSCs, respectively (**SI Figure S20**). The external quantum efficiency (EQE) spectra and integrated J_{sc} values calculated with a wavelength range of 350 and 900 nm show small discrepancies, possibly stemming from the wavelength loss below 350 nm.

To further evaluate the quality of junction and to identify the dominant recombination process in the PSCs, the ideality factors of the PSCs are calculated by extracting the slope of the V_{oc} *vs.* L_n (light intensity) plot (**Figure 4d**).[59,60] The PSC treated with *m*-CF_3 RPP showed an ideality factor of 1.30, whereas the PSC treated with *p*-CF_3 RPP showed a value of 1.53, which indicates that the *m*-CF_3-treated PSCs are less limited by trap-assisted recombination. Additionally, the result of electrochemical impedance spectroscopy by fitting Nyquist plot shows the similar results of ideality factors in PSCs. The impedance spectroscopy proved that PSC treated recombination resistance increased in the order of pristine 3D perovskite, *p*-CF_3-treated PSC, and *m*-CF_3-treated PSCs (**SI Figure S21**). This result also indicates that the *m*-CF_3-treated PSC effectively suppressed recombination losses, resulting in an increase of V_{oc} and the fill-factor (FF). In addition, the built-

in potential (V_{bi}) values of the PSCs were obtained by a Mott-Schottky analysis using the following equation:

$$\frac{1}{C^2} = \frac{2}{\varepsilon\varepsilon_0 eAN_d}(V_{bi} - V)$$

, where C, A and N_d are correspondingly the capacitance, the active area of the PSCs, and the doping concentration. The V_{bi} values of the devices are estimated by determining the intercept of the linear fitted region from the C^{-2} *vs*. V plots. The V_{bi} values of the pristine PSC, *m*-CF_3-RPP-treated PSC, and *p*-CF_3-RPP-treated PSC are estimated to be 0.95, 1.00, and 0.97 V, respectively (**Figure 4e**). The Mott–Schottky plots show that the introduction of the 2D/3D perovskite junction slightly increases V_{bi} compared with pristine device.

Furthermore, the PSCs treated with *m*-CF_3 RPP exhibit significantly enhanced device stability against humidity, maintaining 85% of the initial PCE after 385 hours at a temperature of 25 °C and relative humidity of 65%, as shown in **Figure 5a**. The *p*-CF_3-RPP-treated PSCs also shows enhanced stability against humidity, but lower stability compared to the *m*-CF_3 RPP-treated PSCs. The outcomes of enhanced device stability against humidity can be attributed to the hydrophobicity of the RPP with fluorinated spacer ligands.[35,61] The hydrophobicity of the RPP-treated perovskites are evaluated by measuring the contact angles of water droplets on the films. After the *m*-CF_3 RPP and *p*-CF_3 RPP treatments on top of the 3D perovskite, the contact angles increase from 55.1° to 65.5° and 62.8°, respectively. Furthermore, the optical absorbance spectra of the *m*-CF_3-RPP-treated film showed negligible changes after 150 hours of storage at a relative humidity of 65%, whereas the pristine 3D perovskite showed a significant decrease in the intensity across the entire wavelength range (**Figure 5b**). Furthermore, the *m*-CF_3-treated PSCs show an improved stability against light illumination, maintaining 78% of the initial PSC even after 1100 hours in a N_2 ambient condition under 1-Sun illumination (**SI Figure S22**).[31,33]

Conclusions

In summary, two types of chemically similar but distinct structural isomers, *meta*- CF_3 and *para*-CF_3 groups linked to PEAI, were systematically investigated as interface modifiers. Compared to *p*-CF_3 RPP, the *m*-CF_3 RPP shows a higher interlayer molecule dipole moment, and highly oriented crystal growth with the favorable intermolecular interaction, which may enhance the dissociation of 2D excitons and the out-of-plane transport of the charge carriers to the HTL. Changes in surface dipoles may also explain the shift of band alignments, that shall affect in turn the device properties. The formation of the phase-pure (n = 1) *m*-CF_3 RPP on 3D perovskite film demonstrates the effective suppression of non-radiative recombination and improved carrier lifetimes owing to the passivation of uncoordinated-Pb related defects on the 3D perovskite surface. As a result, the *m*-CF_3-RPP-treated PSCs exhibited a significantly improved PCE up to 22.4%. Furthermore, the *m*-CF_3-RPP-treated PSCs not only show improved stability against humidity owing to the increased hydrophobicity with additional fluorine functional groups, but also excellent operational stability under 1-Sun illumination. These results suggest that the fabrication of stable PSCs while overcoming the vulnerability to humidity of 3D perovskites through fluorinated RPP spacers. Moreover, on top of the multiple fluorine atoms on aromatic spacers, we show that the position of fluorinated groups can further improve the humidity stability of devices. This structural isomer strategy can also be applied to other types of RPP ligands, thus opening an effective pathway by which to improve the performance and stability outcomes of PSCs.

EXPERIMENTAL SECTION

Chemicals: 2-(3-trifluoromethylphenyl)ethanamine and (2-(4-trifluoromethylphenyl)ethanamine (98%) were purchased from J&K Chemical Ltd. Formamidinium lead iodide perovskite ($FAPbI_3$) and Methylammonium lead bromide perovskite ($MAPbBr_3$) powders were purchased from Sharechem. Lead iodide (99.999%) were purchase form Alfa Aesar. Cesium chloride (99.9%) and all solvents used in this study, including dimethylformamide (anhydrous 99.8%), dimethylsulfoxide (anhydrous 99.9%), chlorobenzene (anhydrous 99.7%)) and 2-propanol (anhydrous 99.5%), were purchased from Merck.

Materials synthesis: All the chemicals were used without further purification. 15 mL of (2-(3-trifluoromethylphenyl)ethanamine and (2-(4-trifluoromethylphenyl)ethanamine were firstly dissolved in 200 mL of methanol in a flask in an ice bath, respectively. Then 20 mL of HI aqueous solutions (55 wt%, Sigma Aldrich) were dropped under continuous stirring. After reaction for 6 hr, the solvents of the obtained solutions were removed by vacuum rotary evaporation. The crude precipitates were gradually washed by cold diethyl ether for several times until white powders formed. Finally, both powders were completely dried in vacuum at 65 °C overnight.

Device fabrication: Patterned ITO/glass substrates (AMG Inc.) were sequentially sonicated by using acetone, isopropanol, and deionized water. The cleaned substrates were treated by O_2 plasma for 5 min. A SnO_2 solution were prepared by diluting SnO_2 colloidal solution (15% in H_2O colloidal dispersion, Alfa Aesar) with deionized water (1:4 of volume ratio). The SnO_2 solution were then spin coated at 4000 rpm for 30 s, followed by an annealing at 100 °C for 10 min. Before coating perovskite solution, the substrates with SnO_2 were treated by UV-ozone for 15 min. A precursor solution of perovskite was prepared by adding 949.47 mg of $FAPbI_3$, 37.814 mg of $MAPbBr_3$, 98.4 mg of PbI_2, 13.3 mg of CsCl , 19 mg of MACl in 263 μl of DSMO and 1050 μl of DMF. The

perovskite films were fabricated by spin-coating perovskite solution on the SnO_2 at 1000 rpm 10 s and 5000 rpm for 25 s. The chlorobenzene (CB) was dripped on the substrate at the end of 10 s. The substrates were annealed at 150 °C for 10 min and were subsequently annealed at 100 °C for 10 min. The samples were cooled down to room temperature. For interface treatment with RPPs, 3 mg of *m*-CF_3-PEAI in 1ml of IPA solution and 3 mg of *p*-CF_3-PEAI in 1 ml of IPA solution were prepared, respectively. The substrates were pre-heated at 75 °C for 5 min. The prepared solutions were poured on the pre-heated substrates at 5000 rpm for 20 s and then annealed 100 °C for 10 min. For HTL, Spiro-MeOTAD solution was prepared by dissolving 128 mg of Spiro-MeOTAD in 1.3 ml of chlorobenzene. 50.4 μl of 4-tert-butyl pyridine, 29 μl of Li-TFSI solution (520 mg of Li-TFSI in 1ml of acetonitrile) and 12.6μl of Co-TFSI solution (375mg of FK209 Co-TFSI in 1 ml of acetonitrile) were added into prepared Spiro-MeOTAD solution as a dopant. The HTL was deposited on the perovskite film with 2D/3D heterostructure by spin-coating the Spiro-MeOTAD solution at 3000 rpm for 30 s. The Finally, the substrates were moved to a vacuum chamber for evaporation deposition of 50 nm Au films at a rate of 0.3 Å□s^{-1}. For encapsulation, the samples were moved to a N_2-filled glove box and encapsulated using UV-curable resin (Nagase Inc.) and cover glass. For the flexible devices, bare glass substrates were treated with O_2 plasma to remove residual organic contaminant and improve wettability. PDMS layers (Dow Corning, Sylgard 184) were spin-coated to a O_2 plasma treated glass substrate. The PDMS coated substrates were annealed at 70 °C for 10 min and post-cured for 24 hours at 70°C. ITO / 125 μm-thick polyethylene(naphthalate) (PEN) films (Peccel) were attached to PDMS-coated glass. For fabrication process of SnO_2 and perovskite films, the samples were annealed at 135 °C to avoid damage of flexible substrate.

Device characterization: The *J-V* curves were obtained by using a class-AAA solar simulator (Sol 3A 64023A, Oriel) with a sourcemeter (Keithley 2400) equipped with an AM1.5G filter. 1-Sun illumination intensity of 100 mW□cm^{-2} was calibrated using a certified reference Si cell equipped with a KG5 window (91150-KG5, Newport). Scan voltage ranged from 0.1 to 1.2 V in forward scan and from 1.2 to 0.1 V in reverse scan. The scan rate was set as 100 mV□s^{-1}. Active area of device was defined by using an aperture mask (0.0729 cm^{2}). All *J–V* characterization were conducted in a glovebox at room temperature. Humidity stability of perovskite films were performed by using humidity-controlled equipment (Rcom max20). C-AFM results were obtained to examine DC current of 2D RPPs film by using NX10 equipment (Park Systems) with cantilever tip (SD-R30-NCH, Park systems). A voltage bias of 2 V was applied to acquire DC current. The absorbance spectra of perovskite films were measured by using an UV-visible spectrophotometer (Cary 5000 UV-Vis-NIR, Agilent Ltd). A fluoroMax-4spectrofluorometer (Horiba) was used to measure steady-state PL and time resolved PL. A Xe-arc lamp (150 W) and laser with 463 nm wavelength were used as a excitation source for steady-state- and time-resolved-PL measurements, respectively. The XRD spectra were obtained by using D8-Advance (Bruker) with a monochromatic Cu-Kα radiation. GI-WAXS data were acquired using Xeuss 2.0 HR SAXS/WAXS system with an exposure dwell time of 60 s. FE-SEM (Auriga, Carl Zeiss Ltd) was used to acquire top-view SEM images and FE-SEM (Nova Nanolab, FEI) was used to obtain cross-sectional SEM images. XPS and UPS were performed by using an electron spectroscopy instrument (Nexsa) with an incident radiation using the He-I peak (21.22 eV). The EQE spectra were obtained from incident photon to current efficiency test (IQE-200B, Oriel). For SCLC measurement, electrochemical workstation (Autolab320N, Metrohm) was used with a voltage range from 0 to 2 V. EIS were conducted by using Electrochemical workstation (Autolab 320N,

Metrohm) with a white LED (100 mW□cm^{-2}) as light source. Applied frequency ranging from 10^{0} to 10^{6} Hz and bias voltage ranging from 0.0 to 0.8 V with voltage steps of 0.2 V were used during EIS measurement. To evaluate the hydrophilicity of the prepared perovskite film, contact angle measurement (Phoenix-150, SEO) was carried out using 40 μl of water. The operational stability test under 1 Sun illumination was performed using a reliability measurement system (K3600, McScience) which repeatedly measure the PCE every 5 min.

DFT Calculations: Structure optimizations were performed with DFT calculations by using the Vienna ab-initio simulation package (VASP).[62,63] The PBE functional within generalized gradient approximation (GGA) was used for all calculations[64] The outermost I 5*s*, 5*p*; N and C 2*s*, 2*p*; H 1*s*; Pb 6*s*, 6*p*, 5*d*; F 2*s*, 2*p* electrons are treated as valence electrons whose interactions with the remaining ions are modeled by pseudopotentials generated within the projector-augmented wave (PAW) method.[65] An energy cutoff for the plane-wave basis set is set to 500 eV. A 2 × 4 × 4 *k*-point mesh generated by Monkhorst-Pack scheme is used for all relaxation and self-consistent calculations. Energy and force convergence criteria are set as 0.01 meV and 20 meV□Å^{-1}, respectively, to ensure the structure is fully relaxed and converged. To treat the interaction of organic spacer cations, the van der Waals interaction was taken into account with the non-local correlation functional rev-vdW-DF2.[66] The positions of the atoms, the volume of crystal cells, and volume shape were allowed to relax during the structural optimization. The following formula could be used to calculate layer binding energy (E_b), $E_b = \frac{E_{iso}(n) - E_{bulk}(n)}{A}$, where $E_{iso}(n)$ represent the energy of the unit cell of an isolated slab contains *n*-layers of RPPs in vacuum, $E_{bulk}(n)$ is the energy of the unit cell of *n*-layers of RPPs.[67] A is the in-plane area of the bulk unit cell. The larger E_b indicate the stronger binding strength.

The calculations which involved slabs were performed within the DFT as implemented in the SIESTA package with a basis set of finite-range numerical atomic orbitals.[68] Norm-conserving Troullier-Martins pseudopotentials were used for each atomic species to account for the core electrons.[69] $1s^1$, $2s^22p^2$, $2s^22p^3$, $2s^22p^5$, $5s^25p^5$, and $5d^{10}6s^26p^2$ were used as valence electrons for H, C, N, F, I, and Pb, respectively. A polarized double-zeta basis set with an energy shift of 200 meV and a real space mesh grid energy cutoff of 300 Ry were used for the calculations. For band structure calculation on top of optimized bulk structures, the GGA-PBE functional combined including spin-orbit coupling (SOC) with on-site approximation are used. The Brillouin zone was sampled with a 4 × 8 × 8 and 4 × 4 × 1 Monckhorst-Pack grid for bulk and slab systems, respectively. For the high-frequency dielectric constant profiles, slabs based on the respective systems were constructed, and an electric field of 0.01 eV/Å was applied along the [001] direction to compute the relaxed electron densities, as described elsewhere. For polarization density profiles,[70] we used single-point calculations with GGA-PBE functional including SOC on top of rev-vdw-DF2 optimized structures. The fully relaxed bulk structures were used to construct the slabs with three repeated unit cells, as shown in **SI Figure S5**.

ASSOCIATED CONTENT

Supporting Information

NMR data, additional SEM images, DFT optimized atomistic structures, ADF simulated molecular structure, XRD pattern, XPS, UPS spectra, device performance depending on concentration of organic salt Light stability data (PDF)

AUTHOR INFORMATION

Corresponding Author

M. Choi - Department of Mechanical Engineering, Seoul National University, Global Frontier Center for Multiscale Energy Systems, Seoul National University, Seoul 08826, Republic of Korea

ORCID: 0000-0003-2019-3615

E-mail: mchoi@snu.ac.kr,

J. Xi - Key Laboratory for Physical Electronics and Devices of the Ministry of Education & Shaanxi Key Lab of Information Photonic Technique, School of Electronic Science and Engineering, Xi'an Jiaotong University, No.28, Xianning West Road, Xi'an, 710049, China

ORCID: 0000-0001-6600-4862

E-mail: jun.xi@xjtu.edu.cn

Y. S. Lee - Department of Mechanical Engineering, Seoul National University, Inter-University Semiconductor Research Center, Seoul National University, Seoul 08826, Republic of Korea

ORCID: 0000-0002-2289-109X

Email: leeyunseog@snu.ac.kr

Authors

Junseop Byeon - Department of Mechanical Engineering, Seoul National University, Global Frontier Center for Multiscale Energy Systems, Seoul National University, Seoul 08826, Republic of Korea

Seong Ho Cho - Department of Mechanical Engineering, Seoul National University, Inter-University Semiconductor Research Center, Seoul National University, Seoul 08826, Republic of Korea

Junke Jiang - University of Rennes, ENSCR, CNRS, ISCR, UMR 6226, F-35000 Rennes, France

Jihun Jang - Global Frontier Center for Multiscale Energy Systems, Seoul National University, Seoul 08826, Republic of Korea

Claudine Katan - University of Rennes, ENSCR, CNRS, ISCR, UMR 6226, F-35000 Rennes, France

Jacky Even - Univ Rennes, INSA Rennes, CNRS, Institut FOTON - UMR 6082, F-35000 Rennes, France

Author Contributions

J.B. and S.H.C. contributed equally to this paper.

Notes

The authors declare no competing financial interest.

ACKNOWLEDGMENT

This work was supported by the Global Frontier R&D Program of the Center for Multiscale Energy Systems, the National Research Foundation (NRF) under the Ministry of Education, Science and Technology, Korea (2012M3A6A7054855, 2022R1A6A3A13065166, 2022M3H4A1A03074093, RS-2022-00154545, and NRF-2020R1C1C1005880) *via* Institute of Advanced Machines and Design at Seoul National University (SNU) and SNU Creative-Pioneering Researchers Program via Institute of Engineering Research at SNU, and the European Union's Horizon 2020 research and innovation program under grant agreement No. 861985 (PeroCUBE). J. Xi would like to acknowledge the National Natural Science Foundation of China (Grant No. 62205264), and Xi'an Jiaotong University Young Talents Support Program (11302291010704).

REFERENCES

1. Huang, H.; Bodnarchuk, M. I.; Kershaw, S. V.; Kovalenko, M. V.; Rogach, A. L., Lead Halide Perovskite Nanocrystals in the Research Spotlight: Stability and Defect Tolerance. *ACS Energy Lett*. **2017**, *2* (9), 2071-2083.

2. Chen, Y.; Yi, H. T.; Wu, X.; Haroldson, R.; Gartstein, Y. N.; Rodionov, Y. I.; Tikhonov, K. S.; Zakhidov, A.; Zhu, X. Y.; Podzorov, V., Extended carrier lifetimes and diffusion in hybrid perovskites revealed by Hall effect and photoconductivity measurements. *Nat. Commun*. **2016**, *7* (1), 12253.

3. Eperon, G. E.; Stranks, S. D.; Menelaou, C.; Johnston, M. B.; Herz, L. M.; Snaith, H. J., Formamidinium lead trihalide: a broadly tunable perovskite for efficient planar heterojunction solar cells. *Energy Environ. Sci*. **2014**, *7* (3), 982-988.

4. Kim, M.; Jeong, J.; Lu, H.; Lee, T. K.; Eickemeyer, F. T.; Liu, Y.; Choi, I. W.; Choi, S. J.; Jo, Y.; Kim, H.-B.; Mo, S.-I.; Kim, Y.-K.; Lee, H.; An, N. G.; Cho, S.; Tress, W. R.; Zakeeruddin, S. M.; Hagfeldt, A.; Kim, J. Y.; Grätzel, M.; Kim, D. S., Conformal quantum dot–SnO_2 layers as electron transporters for efficient perovskite solar cells. *Science* **2022**, *375* (6578), 302-306.

5. Min, H.; Lee, D. Y.; Kim, J.; Kim, G.; Lee, K. S.; Kim, J.; Paik, M. J.; Kim, Y. K.; Kim, K. S.; Kim, M. G.; Shin, T. J.; Il Seok, S., Perovskite solar cells with atomically coherent interlayers on SnO_2 electrodes. *Nature* **2021**, *598* (7881), 444-450.

6. Aristidou, N.; Eames, C.; Sanchez-Molina, I.; Bu, X.; Kosco, J.; Islam, M. S.; Haque, S. A., Fast oxygen diffusion and iodide defects mediate oxygen-induced degradation of perovskite solar cells. *Nat. Commun*. **2017**, *8* (1), 15218.

7. Yun, J. S.; Kim, J.; Young, T.; Patterson, R. J.; Kim, D.; Seidel, J.; Lim, S.; Green, M. A.; Huang, S.; Ho-Baillie, A., Humidity-Induced Degradation via Grain Boundaries of $HC(NH_2)_2PbI_3$ Planar Perovskite Solar Cells. *Adv. Funct. Mater.* **2018**, *28* (11), 1705363.

8. Domanski, K.; Alharbi, E. A.; Hagfeldt, A.; Grätzel, M.; Tress, W., Systematic investigation of the impact of operation conditions on the degradation behaviour of perovskite solar cells. *Nat. Energy* **2018**, *3* (1), 61-67.

9. Li, N.; Luo, Y.; Chen, Z.; Niu, X.; Zhang, X.; Lu, J.; Kumar, R.; Jiang, J.; Liu, H.; Guo, X.; Lai, B.; Brocks, G.; Chen, Q.; Tao, S.; Fenning, D. P.; Zhou, H., Microscopic Degradation in Formamidinium-Cesium Lead Iodide Perovskite Solar Cells under Operational Stressors. *Joule* **2020**, *4* (8), 1743-1758.

10. Cho, S. H.; Byeon, J.; Jeong, K.; Hwang, J.; Lee, H.; Jang, J.; Lee, J.; Kim, T.; Kim, K.; Choi, M.; Lee, Y. S., Investigation of Defect-Tolerant Perovskite Solar Cells with Long-Term Stability via Controlling the Self-Doping Effect. *Adv. Energy Mater.* **2021**, *11* (17), 2100555.

11. Motti, S. G.; Meggiolaro, D.; Barker, A. J.; Mosconi, E.; Perini, C. A. R.; Ball, J. M.; Gandini, M.; Kim, M.; De Angelis, F.; Petrozza, A., Controlling competing photochemical reactions stabilizes perovskite solar cells. *Nat. Photonics* **2019**, *13* (8), 532-539.

12. Kwak, K.; Lim, E.; Ahn, N.; Heo, J.; Bang, K.; Kim, S. K.; Choi, M., An atomistic mechanism for the degradation of perovskite solar cells by trapped charge. *Nanoscale* **2019**, *11* (23), 11369-11378.

13. Ahn, N.; Kwak, K.; Jang, M. S.; Yoon, H.; Lee, B. Y.; Lee, J.-K.; Pikhitsa, P. V.; Byun, J.; Choi, M., Trapped charge-driven degradation of perovskite solar cells. *Nat. Commun* **2016**, *7* (1), 13422.

14. Wu, J.; Shi, J.; Li, Y.; Li, H.; Wu, H.; Luo, Y.; Li, D.; Meng, Q., Quantifying the Interface Defect for the Stability Origin of Perovskite Solar Cells. *Adv. Energy Mater.* **2019**, *9* (37), 1901352.

15. Byeon, J.; Kim, J.; Kim, J.-Y.; Lee, G.; Bang, K.; Ahn, N.; Choi, M., Charge Transport Layer-Dependent Electronic Band Bending in Perovskite Solar Cells and Its Correlation to Light-Induced Device Degradation. *ACS Energy Lett.* **2020**, *5* (8), 2580-2589.

16. Di Girolamo, D.; Phung, N.; Kosasih, F. U.; Di Giacomo, F.; Matteocci, F.; Smith, J. A.; Flatken, M. A.; Köbler, H.; Turren Cruz, S. H.; Mattoni, A.; Cinà, L.; Rech, B.; Latini, A.; Divitini, G.; Ducati, C.; Di Carlo, A.; Dini, D.; Abate, A., Ion Migration-Induced Amorphization and Phase Segregation as a Degradation Mechanism in Planar Perovskite Solar Cells. *Adv. Energy Mater* **2020**, *10* (25), 2000310.

17. Shao, Y.; Fang, Y.; Li, T.; Wang, Q.; Dong, Q.; Deng, Y.; Yuan, Y.; Wei, H.; Wang, M.; Gruverman, A.; Shield, J.; Huang, J., Grain boundary dominated ion migration in polycrystalline organic–inorganic halide perovskite films *Energy Environ. Sci* **2016**, *9* (5), 1752-1759.

18. Jeong, K.; Byeon, J.; Jang, J.; Ahn, N.; Choi, M., Pulsatile therapy for perovskite solar cells. *Joule* **2022**, *6* (5), 1087-1102.

19. Niu, T.; Lu, J.; Jia, X.; Xu, Z.; Tang, M.-C.; Barrit, D.; Yuan, N.; Ding, J.; Zhang, X.; Fan, Y.; Luo, T.; Zhang, Y.; Smilgies, D.-M.; Liu, Z.; Amassian, A.; Jin, S.; Zhao, K.; Liu, S., Interfacial Engineering at the 2D/3D Heterojunction for High-Performance Perovskite Solar Cells. *Nano Lett.* **2019**, *19* (10), 7181-7190.

20. Zheng, X.; Hou, Y.; Bao, C.; Yin, J.; Yuan, F.; Huang, Z.; Song, K.; Liu, J.; Troughton, J.; Gasparini, N.; Zhou, C.; Lin, Y.; Xue, D.-J.; Chen, B.; Johnston, A. K.; Wei, N.; Hedhili, M. N.; Wei, M.; Alsalloum, A. Y.; Maity, P.; Turedi, B.; Yang, C.; Baran, D.; Anthopoulos, T. D.; Han,

Y.; Lu, Z.-H.; Mohammed, O. F.; Gao, F.; Sargent, E. H.; Bakr, O. M., Managing grains and interfaces via ligand anchoring enables 22.3%-efficiency inverted perovskite solar cells. *Nat. Energy* **2020**, *5* (2), 131-140.

21. Mao, L.; Stoumpos, C. C.; Kanatzidis, M. G., Two-Dimensional Hybrid Halide Perovskites: Principles and Promises. *J. Am. Chem. Soc.* **2019**, *141* (3), 1171-1190.

22. Tsai, H.; Nie, W.; Blancon, J.-C.; Stoumpos, C. C.; Asadpour, R.; Harutyunyan, B.; Neukirch, A. J.; Verduzco, R.; Crochet, J. J.; Tretiak, S.; Pedesseau, L.; Even, J.; Alam, M. A.; Gupta, G.; Lou, J.; Ajayan, P. M.; Bedzyk, M. J.; Kanatzidis, M. G.; Mohite, A. D., High-efficiency two-dimensional Ruddlesden–Popper perovskite solar cells. *Nature* **2016**, *536* (7616), 312-316.

23. Xi, J.; Byeon, J.; Kim, U.; Bang, K.; Han, G. R.; Kim, J.-Y.; Yoon, J.; Dong, H.; Wu, Z.; Divitini, G.; Xi, K.; Park, J.; Lee, T.-W.; Kim, S. K.; Choi, M.; Lee, J. W., Abnormal spatial heterogeneity governing the charge-carrier mechanism in efficient Ruddlesden–Popper perovskite solar cells. *Energy Environ. Sci.* **2021**, *14* (9), 4915-4925.

24. Xi, J.; Spanopoulos, I.; Bang, K.; Xu, J.; Dong, H.; Yang, Y.; Malliakas, C. D.; Hoffman, J. M.; Kanatzidis, M. G.; Wu, Z., Alternative Organic Spacers for More Efficient Perovskite Solar Cells Containing Ruddlesden–Popper Phases. *J. Am. Chem. Soc.* **2020**, *142* (46), 19705-19714.

25. Lin, Y.; Fang, Y.; Zhao, J.; Shao, Y.; Stuard, S. J.; Nahid, M. M.; Ade, H.; Wang, Q.; Shield, J. E.; Zhou, N.; Moran, A. M.; Huang, J., Unveiling the operation mechanism of layered perovskite solar cells. *Nat. Commun.* **2019**, *10* (1), 1008.

26. Pedesseau, L.; Sapori, D.; Traore, B.; Robles, R.; Fang, H.-H.; Loi, M. A.; Tsai, H.; Nie, W.; Blancon, J.-C.; Neukirch, A.; Tretiak, S.; Mohite, A. D.; Katan, C.; Even, J.; Kepenekian, M., Advances and Promises of Layered Halide Hybrid Perovskite Semiconductors. *ACS Nano* **2016**,

10 (11), 9776-9786; S. Sidhik et al. Deterministic fabrication of 3D/2D perovskite bilayer stacks for durable and efficient solar cells, *Science* **2022**, 377 (6613), 1425-1430

27. Straus, D. B.; Kagan, C. R., Electrons, Excitons, and Phonons in Two-Dimensional Hybrid Perovskites: Connecting Structural, Optical, and Electronic Properties. *J. Phys. Chem. Lett.* **2018**, *9* (6), 1434-1447.

28. Zhang, X.; Wu, G.; Fu, W.; Qin, M.; Yang, W.; Yan, J.; Zhang, Z.; Lu, X.; Chen, H., Orientation Regulation of Phenylethylammonium Cation Based 2D Perovskite Solar Cell with Efficiency Higher Than 11%. *Adv. Energy Mater.* **2018**, *8* (14), 1702498.

29. Grancini, G.; Roldán-Carmona, C.; Zimmermann, I.; Mosconi, E.; Lee, X.; Martineau, D.; Narbey, S.; Oswald, F.; De Angelis, F.; Graetzel, M.; Nazeeruddin, M. K., One-Year stable perovskite solar cells by 2D/3D interface engineering. *Nat. Commun.* **2017**, *8* (1), 15684.

30. Jang, Y.-W.; Lee, S.; Yeom, K. M.; Jeong, K.; Choi, K.; Choi, M.; Noh, J. H., Intact 2D/3D halide junction perovskite solar cells via solid-phase in-plane growth. *Nat. Energy* **2021**, *6* (1), 63-71.

31. Kim, H.; Lee, S.-U.; Lee, D. Y.; Paik, M. J.; Na, H.; Lee, J.; Seok, S. I., Optimal Interfacial Engineering with Different Length of Alkylammonium Halide for Efficient and Stable Perovskite Solar Cells. *Adv. Energy Mater.* **2019**, *9* (47), 1902740.

32. Thrithamarassery Gangadharan, D.; Ma, D., Searching for stability at lower dimensions: current trends and future prospects of layered perovskite solar cells. *Energy Environ. Sci.* **2019**, *12* (10), 2860-2889.

33. Liu, Y.; Akin, S.; Pan, L.; Uchida, R.; Arora, N.; Milić, J. V.; Hinderhofer, A.; Schreiber, F.; Uhl, A. R.; Zakeeruddin, S. M.; Hagfeldt, A.; Dar, M. I.; Grätzel, M., Ultrahydrophobic 3D/2D

fluoroarene bilayer-based water-resistant perovskite solar cells with efficiencies exceeding 22%. *Sci. Adv.* **2019**, *5* (6), eaaw2543.

34. Zhou, Q.; Liang, L.; Hu, J.; Cao, B.; Yang, L.; Wu, T.; Li, X.; Zhang, B.; Gao, P., High-Performance Perovskite Solar Cells with Enhanced Environmental Stability Based on a (p-$FC_6H_4C_2H_4NH_3)_2[PbI_4]$ Capping Layer. *Adv. Energy Mater.* **2019**, *9* (12), 1802595.

35. Zhou, Q.; Xiong, Q.; Zhang, Z.; Hu, J.; Lin, F.; Liang, L.; Wu, T.; Wang, X.; Wu, J.; Zhang, B.; Gao, P., Fluoroaromatic Cation-Assisted Planar Junction Perovskite Solar Cells with Improved V_{oc} and Stability: The Role of Fluorination Position. *Sol. RRL* **2020**, *4* (7), 2000107.

36. Zhang, F.; Kim, D. H.; Lu, H.; Park, J.-S.; Larson, B. W.; Hu, J.; Gao, L.; Xiao, C.; Reid, O. G.; Chen, X.; Zhao, Q.; Ndione, P. F.; Berry, J. J.; You, W.; Walsh, A.; Beard, M. C.; Zhu, K., Enhanced Charge Transport in 2D Perovskites via Fluorination of Organic Cation. *J. Am. Chem. Soc.* **2019**, 141 (14), 5972-5979.

37. Shi, J.; Gao, Y.; Gao, X.; Zhang, Y.; Zhang, J.; Jing, X.; Shao, M., Fluorinated Low-Dimensional Ruddlesden–Popper Perovskite Solar Cells with over 17% Power Conversion Efficiency and Improved Stability. *Adv. Mater.* **2019**, *31* (37), 1901673.

38. Hu, J.; Oswald, I. W. H.; Stuard, S. J.; Nahid, M. M.; Zhou, N.; Williams, O. F.; Guo, Z.; Yan, L.; Hu, H.; Chen, Z.; Xiao, X.; Lin, Y.; Yang, Z.; Huang, J.; Moran, A. M.; Ade, H.; Neilson, J. R.; You, W., Synthetic control over orientational degeneracy of spacer cations enhances solar cell efficiency in two-dimensional perovskites. *Nat. Commun.* **2019**, *10* (1), 1276.

39. Pitaro, M.; Pau, R.; Duim, H.; Mertens, M.; Van Gompel, W. T. M.; Portale, G.; Lutsen, L.; Loi, M. A. Tin-Lead-Metal Halide Perovskite Solar Cells with Enhanced Crystallinity and Efficiency by Addition of Fluorinated Long Organic Cation. *Appl. Phys. Rev.* **2022**, 9, 021407

40. Cai, Y.; Wen, J.; Liu, Z.; Qian, F.; Duan, C.; He, K.; Zhao, W.; Zhan, S.; Yang, S.; Cui, J.; Liu, S., Graded 2D/3D $(CF_3\text{-}PEA)_2FA_{0.85}MA_{0.15}Pb_2I_7/FA_{0.85}MA_{0.15}PbI_3$ heterojunction for stable perovskite solar cell with an efficiency over 23.0%. *J. Energy Chem.* **2022,** *65*, 480-489.

41. Zhou, J.; Li, M.; Wang, S.; Tan, L.; Liu, Y.; Jiang, C.; Zhao, X.; Ding, L.; Yi, C., 2-CF_3-PEAI to eliminate Pb0 traps and form a 2D perovskite layer to enhance the performance and stability of perovskite solar cells. *Nano Energy* **2022,** *95*, 107036.

42. Lee, H. B.; Kumar, N.; Tyagi, B.; Ko, K.-J.; Kang, J.-W., Dimensionality and Defect Engineering Using Fluoroaromatic Cations for Efficiency and Stability Enhancement in 3D/2D Perovskite Photovoltaics. *Sol. RRL* **2021**, *5* (3), 2000589.

43. Qiu, Y.; Liang, J.; Zhang, Z.; Deng, Z.; Xu, H.; He, M.; Wang, J.; Yang, Y.; Kong, L.; Chen, C.-C., Tuning the Interfacial Dipole Moment of Spacer Cations for Charge Extraction in Efficient and Ultrastable Perovskite Solar Cells. *J. Phys. Chem. C* **2021**, *125* (2), 1256-1268.

44. Liu, C.; Yang, Y.; Rakstys, K.; Mahata, A.; Franckevicius, M.; Mosconi, E.; Skackauskaite, R.; Ding, B.; Brooks, K. G.; Usiobo, O. J.; Audinot, J.-N.; Kanda, H.; Driukas, S.; Kavaliauskaite, G.; Gulbinas, V.; Dessimoz, M.; Getautis, V.; De Angelis, F.; Ding, Y.; Dai, S.; Dyson, P. J.; Nazeeruddin, M. K., Tuning structural isomers of phenylenediammonium to afford efficient and stable perovskite solar cells and modules. *Nat. Commun.* **2021**, *12* (1), 6394.

45. Wei, Y.; Audebert, P.; Galmiche, L.; Lauret, J. S.; Deleporte, E., Synthesis, optical properties and photostability of novel fluorinated organic–inorganic hybrid $(R\text{–}NH_3)_2PbX_4$ semiconductors. *J. Phys. D J PHYS D APPL PHYS* **2013**, *46* (13), 135105.

46. Passarelli, J. V.; Fairfield, D. J.; Sather, N. A.; Hendricks, M. P.; Sai, H.; Stern, C. L.; Stupp, S. I., Enhanced Out-of-Plane Conductivity and Photovoltaic Performance in n = 1 Layered Perovskites through Organic Cation Design. *J. Am. Chem. Soc.* **2018,** *140* (23), 7313-7323.

47. Bouduban, M. E. F.; Queloz, V. I. E.; Caselli, V. M.; Cho, K. T.; Kirmani, A. R.; Paek, S.; Roldan-Carmona, C.; Richter, L. J.; Moser, J. E.; Savenije, T. J.; Nazeeruddin, M. K.; Grancini, G., Crystal Orientation Drives the Interface Physics at Two/Three-Dimensional Hybrid Perovskites. *J. Phys. Chem. Lett.* **2019**, 10 (19), 5713-5720.

48. Liu, Z.; Meng, K.; Wang, X.; Qiao, Z.; Xu, Q.; Li, S.; Cheng, L.; Li, Z.; Chen, G., In Situ Observation of Vapor-Assisted 2D–3D Heterostructure Formation for Stable and Efficient Perovskite Solar Cells. *Nano Lett.* **2020**, *20* (2), 1296-1304.

49. Zhou, T.; Lai, H.; Liu, T.; Lu, D.; Wan, X.; Zhang, X.; Liu, Y.; Chen, Y., Highly Efficient and Stable Solar Cells Based on Crystalline Oriented 2D/3D Hybrid Perovskite. *Adv. Mater.* **2019**, *31* (32), 1901242.

50. Garai, R.; Gupta, R. K.; Hossain, M.; Iyer, P. K., Surface recrystallized stable 2D–3D graded perovskite solar cells for efficiency beyond 21%. *J. Mater. Chem. A* **2021**, *9* (46), 26069-26076.

51. Shao, Y.; Xiao, Z.; Bi, C.; Yuan, Y.; Huang, J., Origin and elimination of photocurrent hysteresis by fullerene passivation in $CH_3NH_3PbI_3$ planar heterojunction solar cells. *Nat. Commun.* **2014**, *5* (1), 5784.

52. Menke, S. M.; Ran, N. A.; Bazan, G. C.; Friend, R. H., Understanding Energy Loss in Organic Solar Cells: Toward a New Efficiency Regime. *Joule* **2018**, *2* (1), 25-35.

53. Shockley, W.; Queisser, H. J., Detailed Balance Limit of Efficiency of p- n Junction Solar Cells. *J. Appl. Phys.* **1961**, *32* (3), 510-519.

54. Yang, S.; Dai, J.; Yu, Z.; Shao, Y.; Zhou, Y.; Xiao, X.; Zeng, X. C.; Huang, J., Tailoring Passivation Molecular Structures for Extremely Small Open-Circuit Voltage Loss in Perovskite Solar Cells. *J. Am. Chem. Soc.* **2019**, *141* (14), 5781-5787.

55. Wang, L.; Zhou, H.; Hu, J.; Huang, B.; Sun, M.; Dong, B.; Zheng, G.; Huang, Y.; Chen, Y.; Li, L.; Xu, Z.; Li, N.; Liu, Z.; Chen, Q.; Sun, L.-D.; Yan, C.-H., A Eu3+-Eu2+ ion redox shuttle imparts operational durability to Pb-I perovskite solar cells. *Science* **2019**, *363* (6424), 265-270.

56. Alharbi, E. A.; Krishna, A.; Baumeler, T. P.; Dankl, M.; Fish, G. C.; Eickemeyer, F.; Ouellette, O.; Ahlawat, P.; Škorjanc, V.; John, E.; Yang, B.; Pfeifer, L.; Avalos, C. E.; Pan, L.; Mensi, M.; Schouwink, P. A.; Moser, J.-E.; Hagfeldt, A.; Rothlisberger, U.; Zakeeruddin, S. M.; Grätzel, M., Methylammonium Triiodide for Defect Engineering of High-Efficiency Perovskite Solar Cells. *ACS Energy Lett*. **2021**, *6* (10), 3650-3660.

57. Gharibzadeh, S.; Fassl, P.; Hossain, I. M.; Rohrbeck, P.; Frericks, M.; Schmidt, M.; Duong, T.; Khan, M. R.; Abzieher, T.; Nejand, B. A.; Schackmar, F.; Almora, O.; Feeney, T.; Singh, R.; Fuchs, D.; Lemmer, U.; Hofmann, J. P.; Weber, S. A. L.; Paetzold, U. W., Two birds with one stone: dual grain-boundary and interface passivation enables >22% efficient inverted methylammonium-free perovskite solar cells. *Energy Environ. Sci*. **2021**, *14* (11), 5875-5893.

58. Wang, X.; Rakstys, K.; Jack, K.; Jin, H.; Lai, J.; Li, H.; Ranasinghe, C. S. K.; Saghaei, J.; Zhang, G.; Burn, P. L.; Gentle, I. R.; Shaw, P. E., Engineering fluorinated-cation containing inverted perovskite solar cells with an efficiency of >21% and improved stability towards humidity. *Nat. Commun*. **2021**, *12* (1), 52.

59. Du, T.; Kim, J.; Ngiam, J.; Xu, S.; Barnes, P. R. F.; Durrant, J. R.; McLachlan, M. A., Elucidating the Origins of Subgap Tail States and Open-Circuit Voltage in Methylammonium Lead Triiodide Perovskite Solar Cells. *Adv. Funct. Mater*. **2018**, *28* (32), 1801808.

60. Wu, Y.; Li, X.; Fu, S.; Wan, L.; Fang, J., Efficient methylammonium lead trihalide perovskite solar cells with chloroformamidinium chloride (Cl-FACl) as an additive. *J. Mater. Chem. A* **2019**, *7* (14), 8078-8084.

61. Wang, L.; Zhou, Q.; Zhang, Z.; Li, W.; Wang, X.; Tian, Q.; Yu, X.; Sun, T.; Wu, J.; Zhang, B.; Gao, P., A guide to use fluorinated aromatic bulky cations for stable and high-performance 2D/3D perovskite solar cells: The more fluorination the better? , *J. Energy Chem.* **2022**, *64*, 179-189.

62. Kresse, G.; Furthmüller, J., Efficiency of ab-initio total energy calculations for metals and semiconductors using a plane-wave basis set. *Comput. Mater. Sci.* **1996**, *6* (1), 15-50.

63. Kresse, G.; Furthmüller, J., Efficient iterative schemes for ab initio total-energy calculations using a plane-wave basis set. *Phys. Rev. B.* **1996**, *54* (16), 11169-11186.

64. Perdew, J. P.; Burke, K.; Ernzerhof, M., Generalized Gradient Approximation Made Simple. *Phys. Rev. Lett.* **1996**, *77* (18), 3865-3868.

65. Blöchl, P. E., Projector augmented-wave method. *Phys. Rev. B.* **1994**, *50* (24), 17953-17979.

66. Hamada, I., van der Waals density functional made accurate. *Phys. Rev. B.* **2014**, *89* (12), 121103.

67. Jung, J. H.; Park, C.-H.; Ihm, J., A Rigorous Method of Calculating Exfoliation Energies from First Principles. *Nano Lett.* **2018**, *18* (5), 2759-2765.

68. Soler, J. M.; Artacho E.; Gale J. D.; García A.; Junquera1 J.; Ordejón P.; Sánchez-Portal D., The SIESTA method for ab initio order-N materials simulation. *J. Phys. Condens. Matter.* **2002**, 14, 2745-2779.

69. Troullier, N.; Martins, J. L., Efficient pseudopotentials for plane-wave calculations. *Phys. Rev. B* **1991**, 43, 1993-2006.

70 Traore, B.; Pedesseau, L.; Assam, L.; Che, X.; Blancon, J. C.; Tsai, H.; Nie, W.; Stoumpos, C. C.; Kanatzidis, M. G.; Tretiak, S.; Mohite, A. D.; Even, J.; Kepenekian, M.;

Katan, C., Composite Nature of Layered Hybrid Perovskites: Assessment on Quantum and Dielectric Confinements and Band Alignment. ACS Nano **2018**, 12 (4), 3321-3332.

71 Traore, B.; Basera, P.; Ramadan, A. J.; Snaith, H. J.; Katan, C.; Even, J. A Theoretical Framework for Microscopic Surface and Interface Dipoles, Work Functions, and Valence Band Alignments in 2D and 3D Halide Perovskite Heterostructures, *ACS Energy Letters* **2022**, 7, 349–357.

Table 1. PL peak position, band gap (E_g), excitonic peak (E_{s1}), continuum edges and exciton binding energies (E_b) driven from steady-state PL and UV-VIS absorbance spectra of RPP films

Material	PL (eV)	Band edge (eV)	Excitonic peak (eV)	Continuum edge (eV)	$E_{binding}$(meV)
m-CF_3	2.51	2.59	2.57	2.83	260
p-CF_3	2.30	2.39	2.37	2.65	280

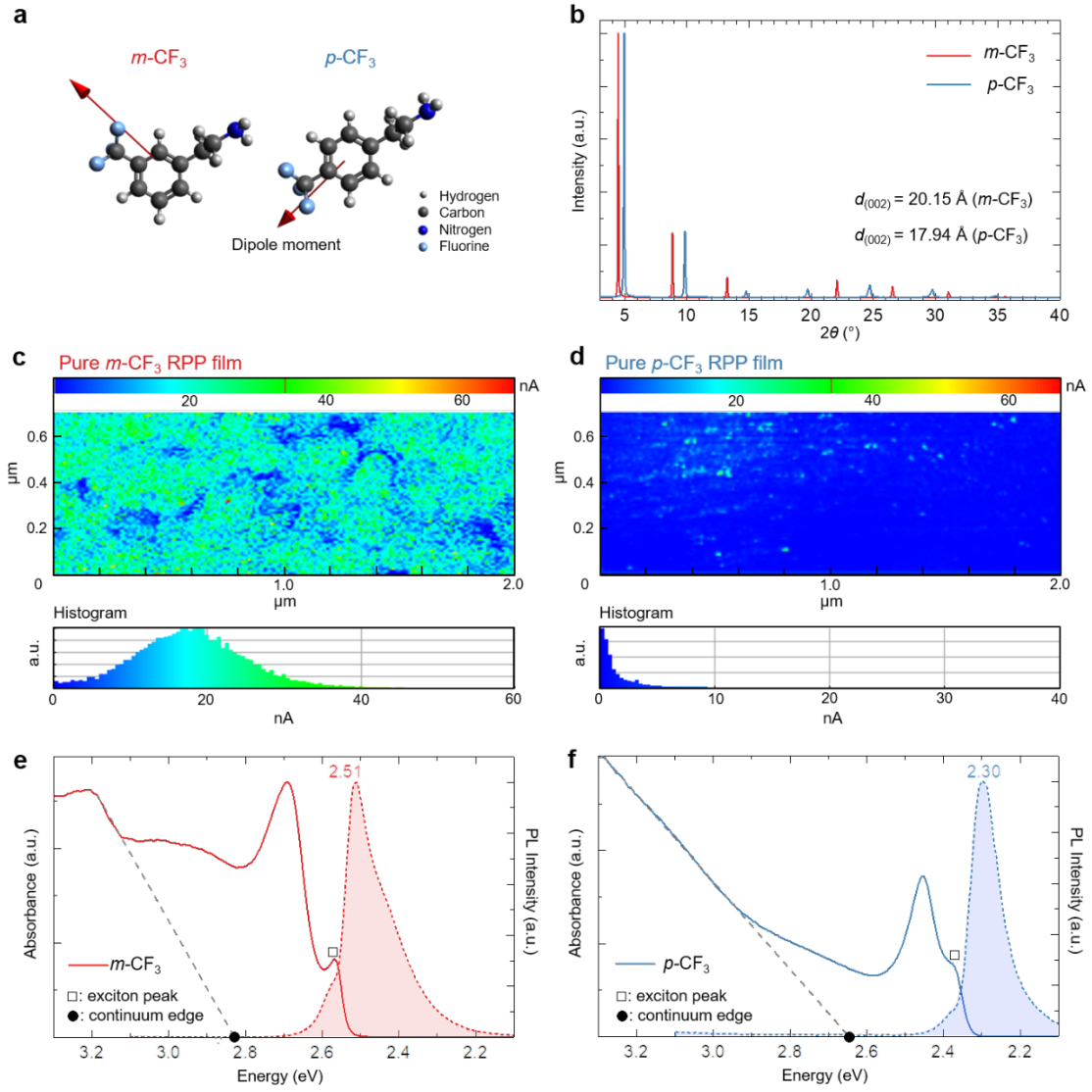

Figure 1. (a) Molecular structure of *m*-CF_3 PEAI and *p*-CF_3 PEAI, respectively. (b) XRD spectra of (*m*-CF_3PEA)$_2$$PbI_4$ and (*p*-CF_3PEA)$_2$$PbI_4$. Spatial map and histogram of current level from C-AFM measurements of (c) *m*-CF_3 PEAI and (d) *p*-CF_3 PEAI films on ITO substrates. Optical absorbance and PL spectra of (e) (*m*-CF_3PEA)$_2$$PbI_4$ and (f) (*p*-CF_3PEA)$_2$$PbI_4$ thin-films on glass substrates.

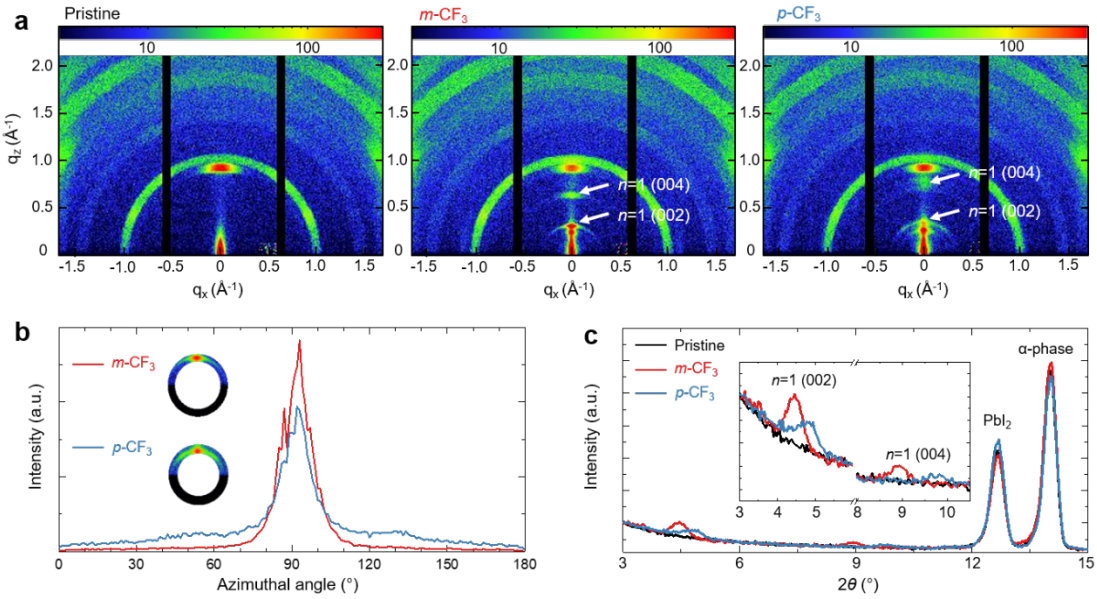

Figure 2. (a) GI-WAXS measurements and (b) Azimuthal angle scans for (002) peak of *m*-CF_3 PEAI treated 2D/3D perovskite films and *p*-CF_3 PEAI treated 2D/3D perovskite films. (c) GI-XRD spectra of pristine 3D perovskite films, *m*-CF_3 PEAI treated, *p*-CF_3 PEAI treated 2D/3D perovskite films. Inset shows peaks corresponding pure RPPs.

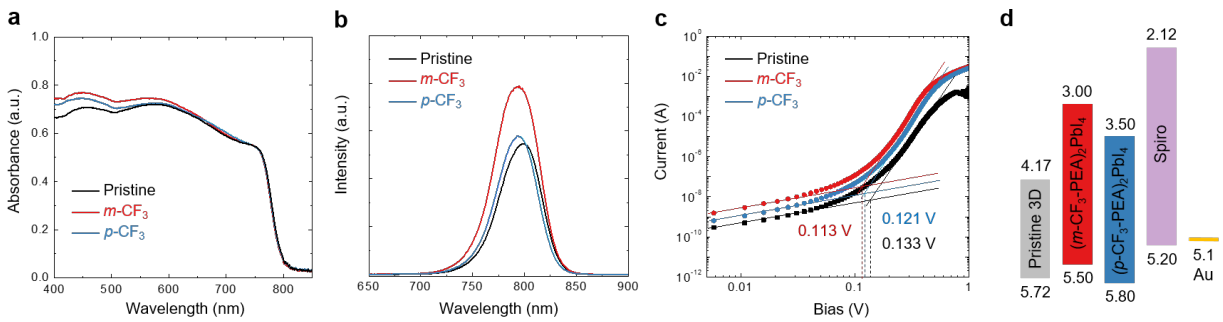

Figure 3. (a) UV-VIS absorbance spectra and (b) steady-state PL spectra of pristine 3D perovskite films, *m*-CF_3-PEAI treated- and *p*-CF_3-PEAI treated 2D/3D perovskite films. (c) *J-V* characteristics from SCLC measurements for electron only device using perovskite films with and without organic ammonium iodide treatment. (d) Schematic energy band alignment diagram of 3D perovskite films and 2D/3D perovskite films.

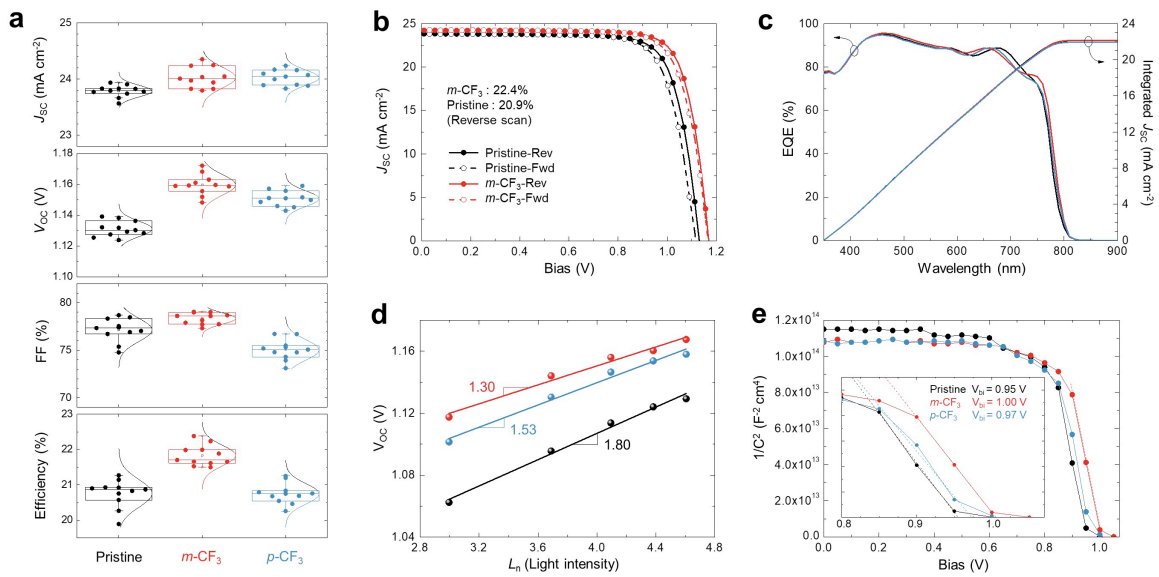

Figure 4. (a) Statistical histogram of *J-V* characteristics of perovskite solar cells with pristine, *m*-CF_3-PEAI treated, *p*-CF_3-PEAI treated perovskite films. (b) *J-V* curves of the best performing solar cells at both reverse and forward scans. Solid lines and dashed lines indicate reverse scans and forward scans, respectively. (c) EQE spectra and integrated photocurrent density curves of the devices. (d) Light intensity dependent V_{oc} profiles of perovskite solar cells with pristine and organic ammonium iodide treated perovskite films. (e) Mott-Schottky plots of perovskite solar cells with pristine perovskite films, *m*-CF_3-PEAI treated- and *p*-CF_3-PEAI treated perovskite films.

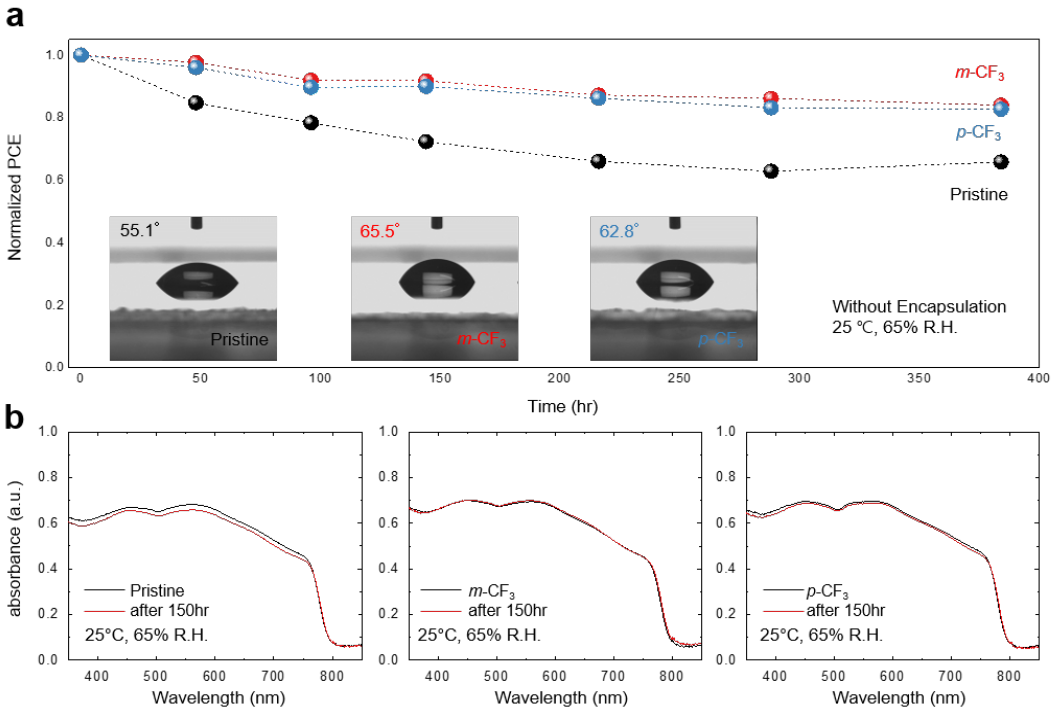

Figure 5. (a) Stability of perovskite solar cells against humidity without encapsulation (25 °C, 65% R.H. storage condition) and pictures of the contact angle measurements of water droplets on pristine 3D perovskite films, *m*-CF_3 PEAI treated, and *p*-CF_3 PEAI treated 2D/3D perovskite films. (b) Changes of absorbance spectra of perovskite films before and after humidity stability tests.

Supporting Information

Structural isomer of fluorinated Ruddlesden-Popper perovskite towards efficient and stable 2D/3D perovskite solar cells

Junseop Byeon[1,2†], Seong Ho Cho[1,6†], Junke Jiang[3], Jihun Jang[2], Claudine Katan[3], Jacky Even[4], Jun Xi[5], Mansoo Choi[1,2]*, Yun Seog Lee[1,6]**

[1]Department of Mechanical Engineering, Seoul National University, Seoul 08826, Republic of Korea

[2]Global Frontier Center for Multiscale Energy Systems, Seoul National University, Seoul 08826, Republic of Korea

[3]Univ of Rennes, ENSCR, CNRS, ISCR, UMR 6226, F-35000 Rennes, France

[4]Univ of Rennes, INSA Rennes, CNRS, Institute FOTON - UMR 6082, F-35000 Rennes, France

[5]Key Laboratory for Physical Electronics and Devices of the Ministry of Education & Shaanxi Key Lab of Information Photonic Technique, School of Electronic Science and Engineering, Xi'an Jiaotong University, No.28, Xianning West Road, Xi'an, 710049, China

[a]Inter-University Semiconductor Research Center, Seoul National University, Seoul 08826, Republic of Korea

* Corresponding authors

E-mail: mchoi@snu.ac.kr, jun.xi@xjtu.edu.cn, leeyunseog@snu.ac.kr

[†]J.B. and S.H.C contributed equally to this paper

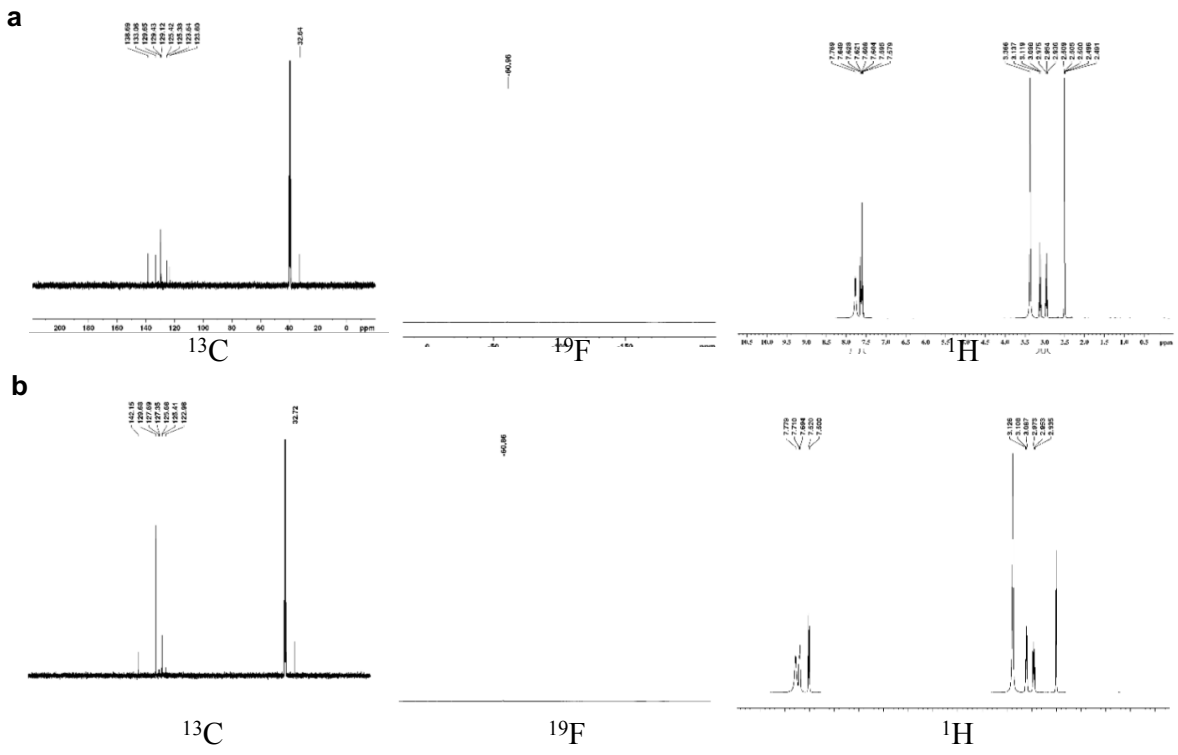

Figure S1. NMR measurement of a) (*m*-CF_3PEA)$_2$$PbI_4$ and b) (*p*-CF_3PEA)$_2$$PbI_4$ films.

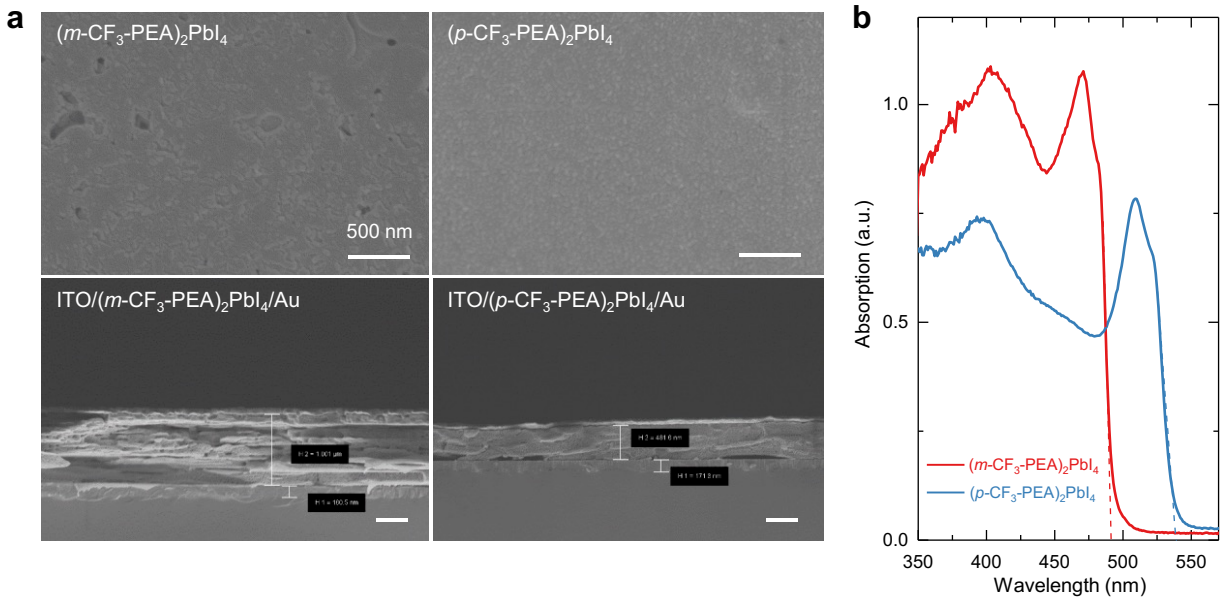

Figure S2. (a) Top surface and cross-sectional SEM images of pure (m-$CF_3PEA)_2PbI_4$ and (p-$CF_3PEA)_2PbI_4$ films. Scale bar, 500 nm. (b) Absorption spectra of pure (m-$CF_3PEA)_2PbI_4$ and (p-$CF_3PEA)_2PbI_4$ films.

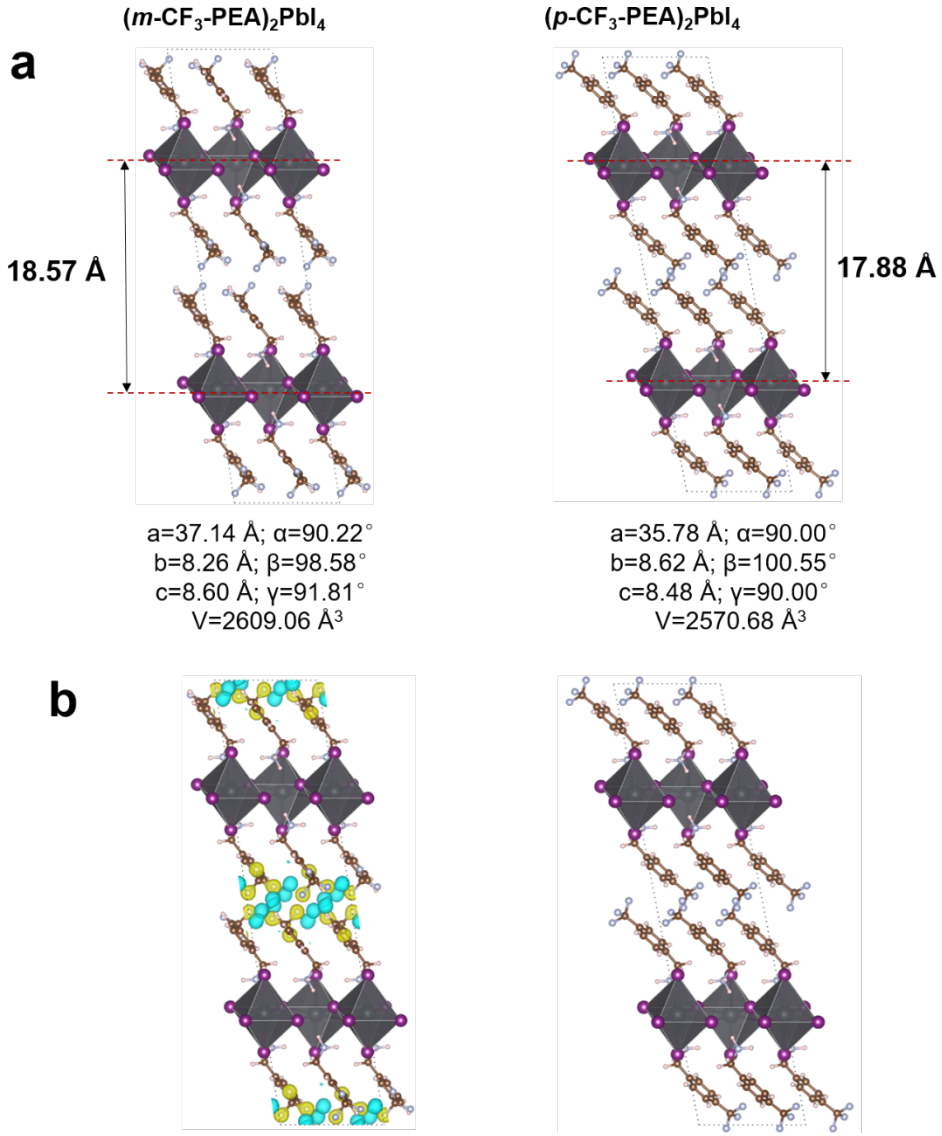

Figure S3. (a) DFT optimized atomistic structures and (b) charge density difference between the whole structure and the hypothetical structure containing one out of the two organic-inorganic layers of (m-CF_3-PEA)$_2$$PbI_4$ (left panels) and (p-CF_3-PEA)$_2$$PbI_4$ (right panels). The yellow and cyan regions indicate the charge accumulation and depletion, respectively, and the isosurface value is 0.25 e□Å^{-3}. This reveals increased inter-molecular hybridization between the m-CF_3-PEA cations in the m-CF_3 RPP, compared to the para isomer.

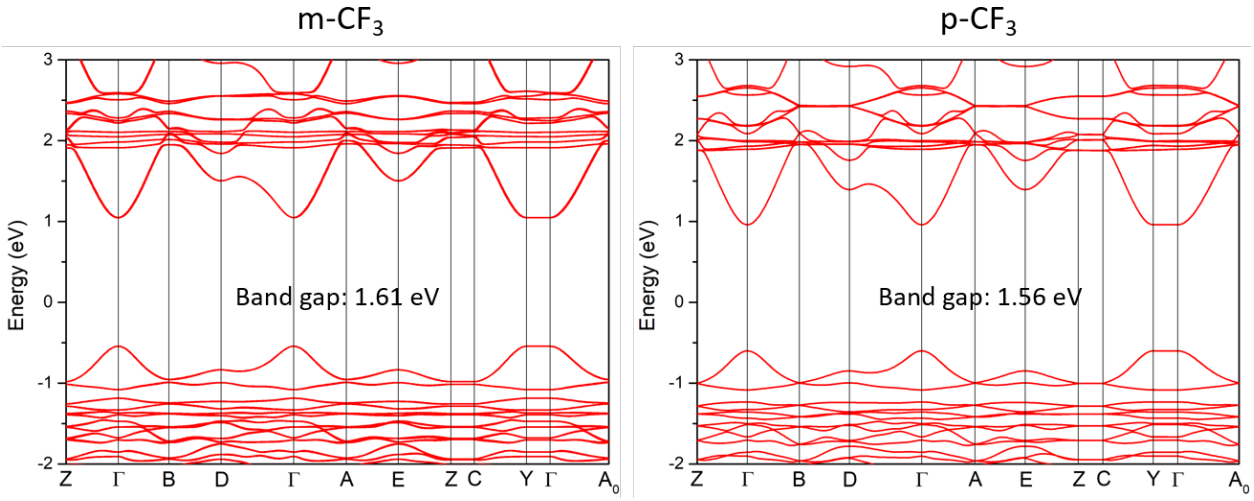

Figure S4. Electronic band structures of the *m*-CF_3 and *p*-CF_3 layered perovskites computed at the PBE level. The x-axis shows the labels of the high symmetry points of the $P2_1/c$ space group Brillouin zone.

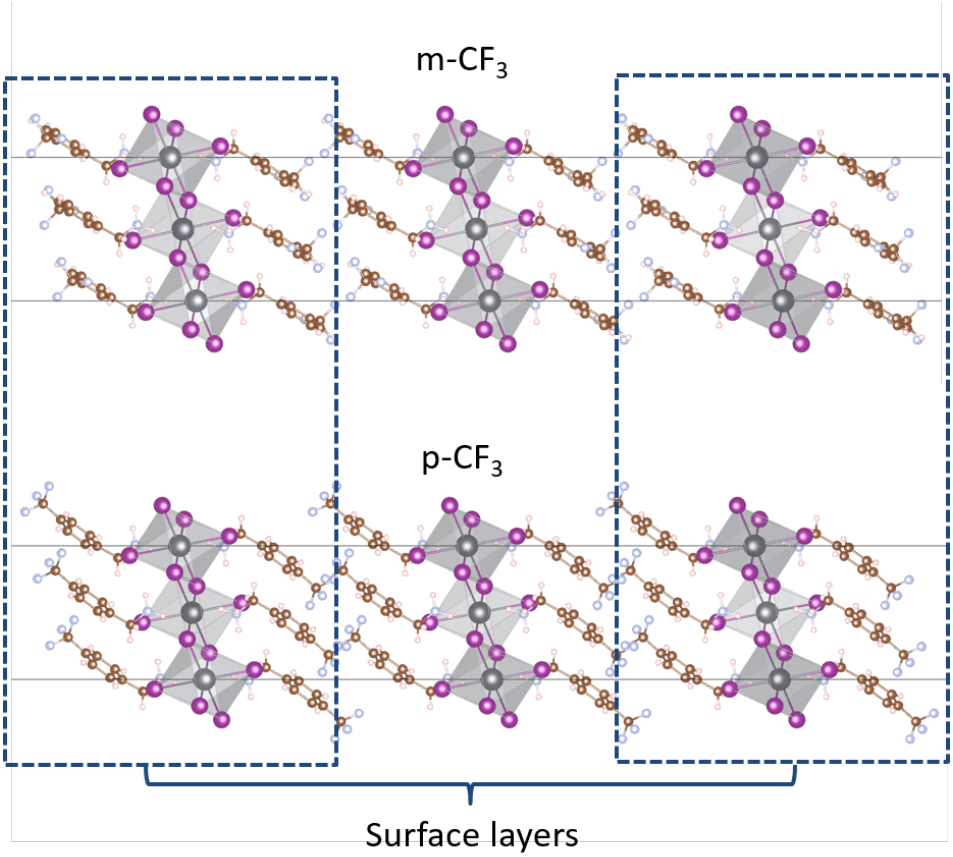

Figure S5. Slab model structures considered for the evaluation of the polarization density profiles along the stacking axes of the *m*-CF_3 and *p*-CF_3 layered perovskites. The slabs contain three perovskite layers. The surface layers within the dashed rectangular boxes are allowed to relax while the central bulk-like regions are kept frozen to the positions of the optimized bulk structures. During structural optimization, only the atomic positions were allowed to relax.

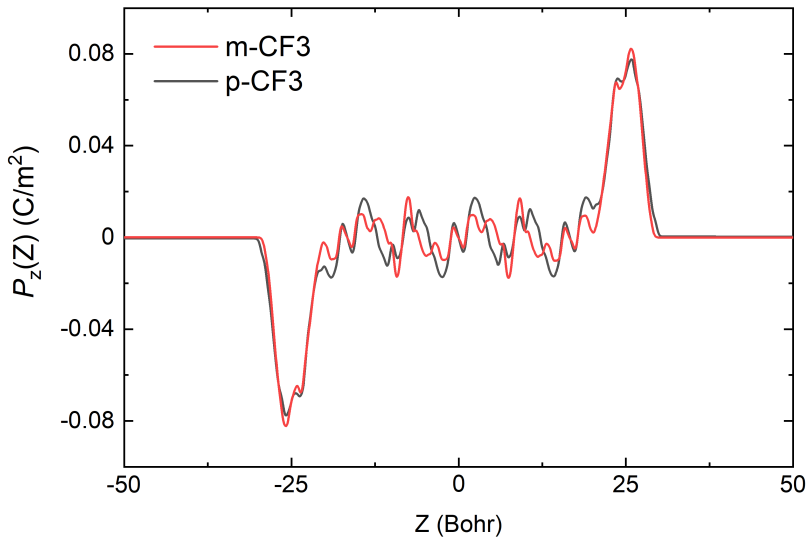

Figure S6. Polarization density profiles of the *m*-CF_3 and *p*-CF_3 layered perovskites along the stacking axes.[1] The surface dipole densities p extracted from the polarization density profiles are equal to 4.84 × 10^{-11} C/m and 5.19 × 10^{-11} C/m for *m*-CF_3 and *p*-CF_3 layered perovskites, respectively. By using the equation $\Delta E_V^{abs} = -1.809 \times 10^{-8}\, \Delta p$, the energy of the valence band maximum of the *m*-CF_3 layered perovskite is predicted to be larger by 0.40 eV than the one of the *p*-CF_3 layered perovskite.

Table S1. VASP simulated molecular structures, dipole moments of *m*-CF_3-PEA^+ and *p*-CF_3-PEA^+. The dipole moments are calculated by the VASP code using the PBE functional, considering the mass centers as the origin.

	m-CF_3 PEA	*p*-CF_3 PEA
Structure	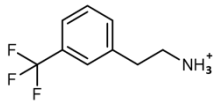 2-(3-trifluromethylphenyl)ethanaminium	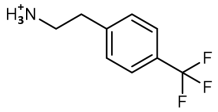 2-(4-(trifluoromethyl)phenyl)ethanaminium
Simulated Molecular Structure	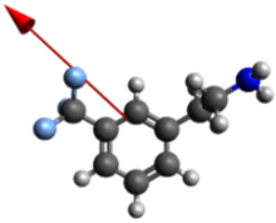	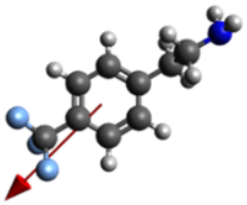
Estimated Dipole Moment μ (Debye)	1.3	0.3

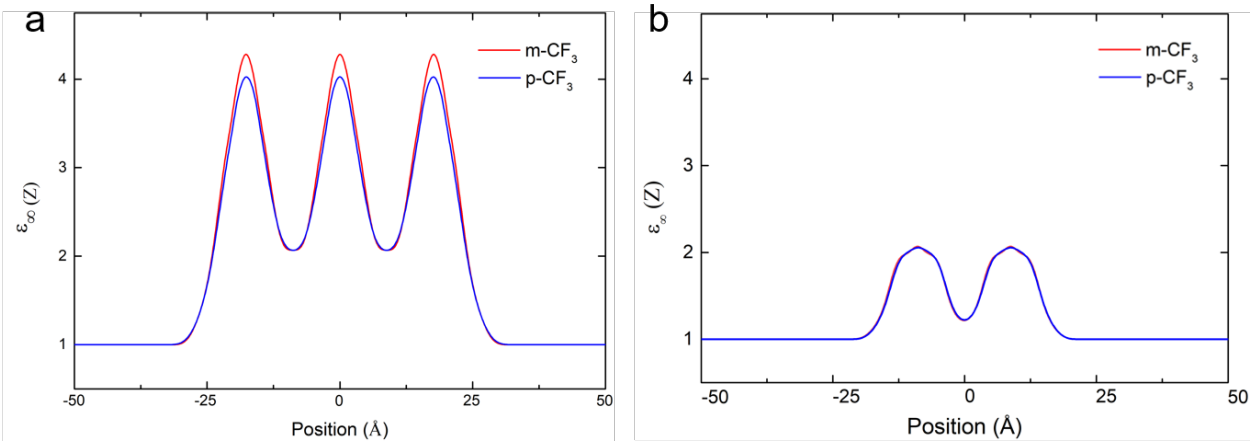

Figure S7. Dielectric profiles computed from slab models[2] for (a) *m*-CF_3 and *p*-CF_3 layered perovskites and (b) the sole spacers *m*-CF_3-PEA (red) and *p*-CF_3-PEA (blue). In the later case, the nitrogen atom are replaced by carbon to avoid charged unit cells.

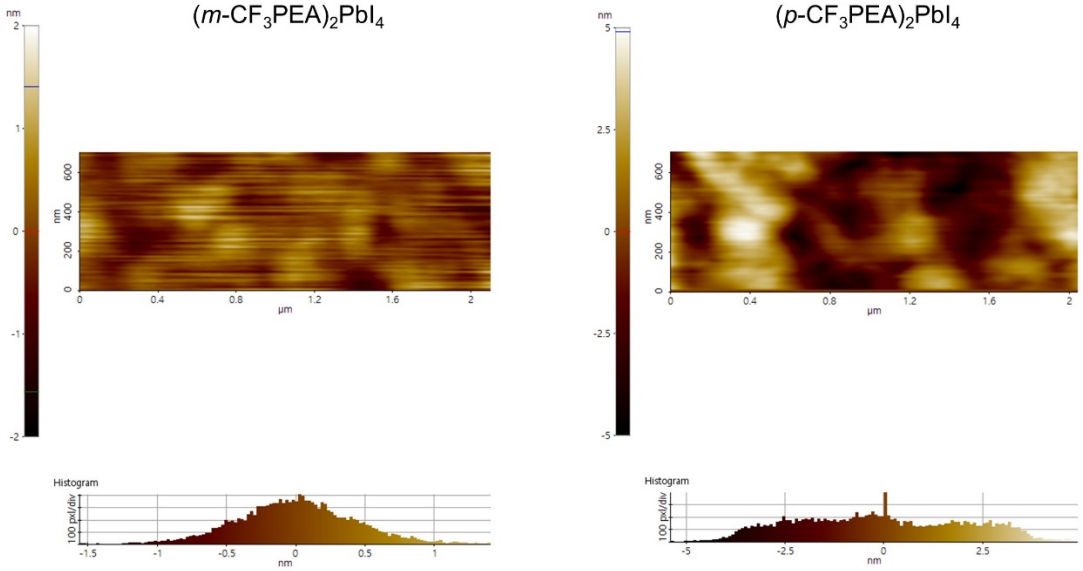

Figure S8. AFM measurement of pure (m-$CF_3PEA)_2PbI_4$ and (p-$CF_3PEA)_2PbI_4$ films

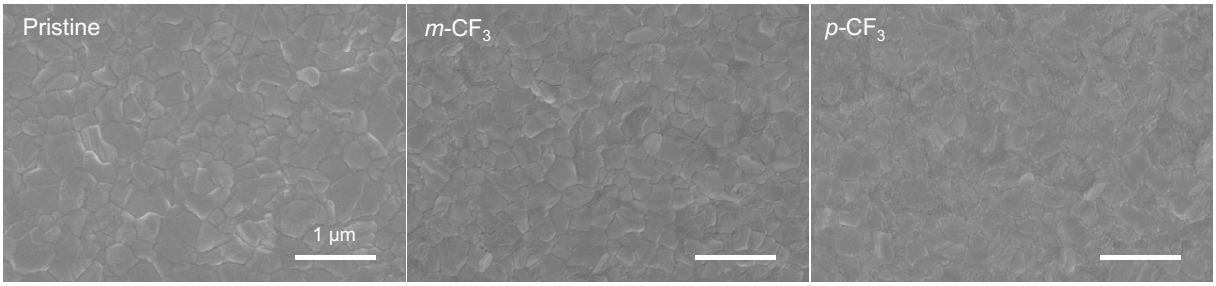

Figure S9. Surface SEM images of the pristine 3D perovskite films, *m*-CF_3 PEAI treated, *p*-CF_3 PEAI treated 2D/3D perovskite films. Scale bar, 1 μm.

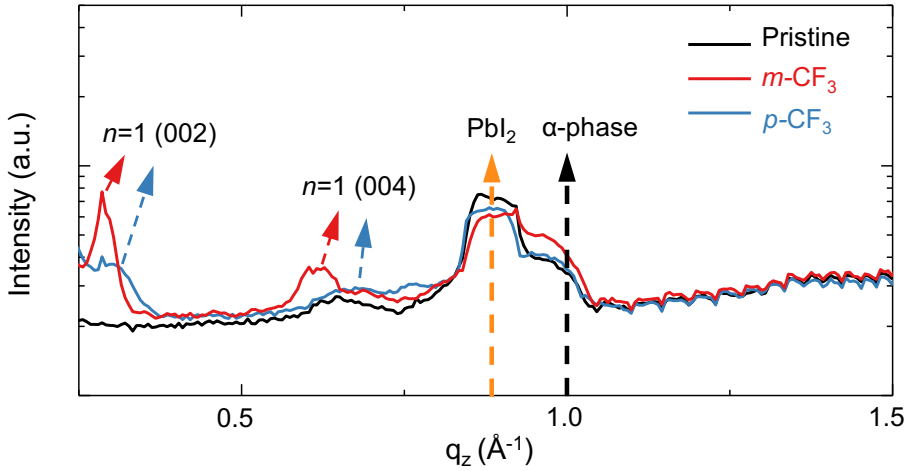

Figure S10. GI-WAXS profiles in out of plane direction of pristine perovskite films, *m*-CF_3 PEAI treated- and *p*-CF_3 PEAI treated perovskite films.

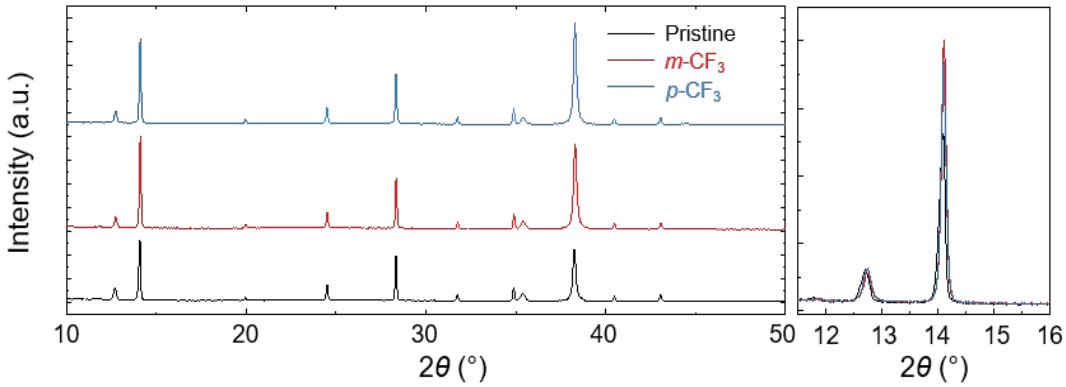

Figure S11. XRD spectra of pristine 3D perovskite films, *m*-CF_3 PEAI treated, *p*-CF_3 PEAI treated 2D/3D perovskite films.

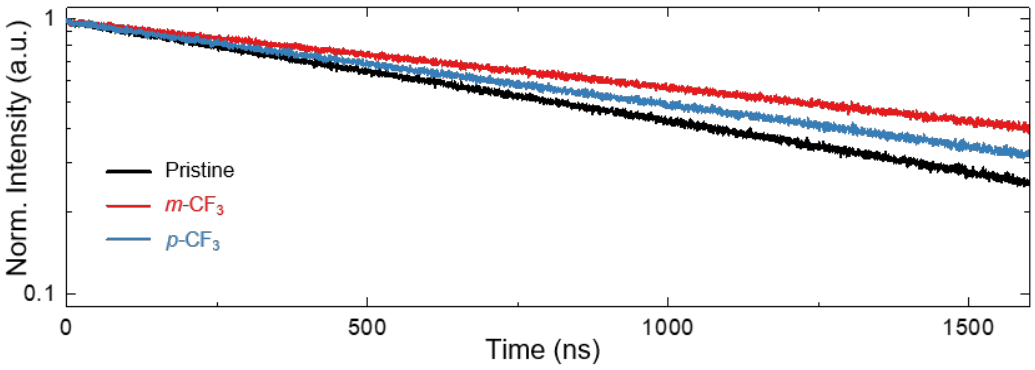

Figure S12. Time resolved PL spectra of pristine 3D perovskite films, *m*-CF_3 PEAI treated, *p*-CF_3 PEAI treated 2D/3D perovskite films.

Table S2. Capacitance (*C*), active area, thickness, dielectric constant, trap filled limit voltage and trap density of perovskite with and without organic ammonium iodide treatment.

Sample	*C* [10^{-9} F]	Active area [cm^2]	Thickness [nm]	ε	V_{TFL} [eV]	N_t [10^{15} cm^{-3}]
Pristine	8.06	0.1825	550	27.47	0.133	1.34
m-CF_3	7.64	0.1825	580	27.46	0.113	1.02
p-CF_3	8.20	0.1825	580	29.47	0.121	1.17

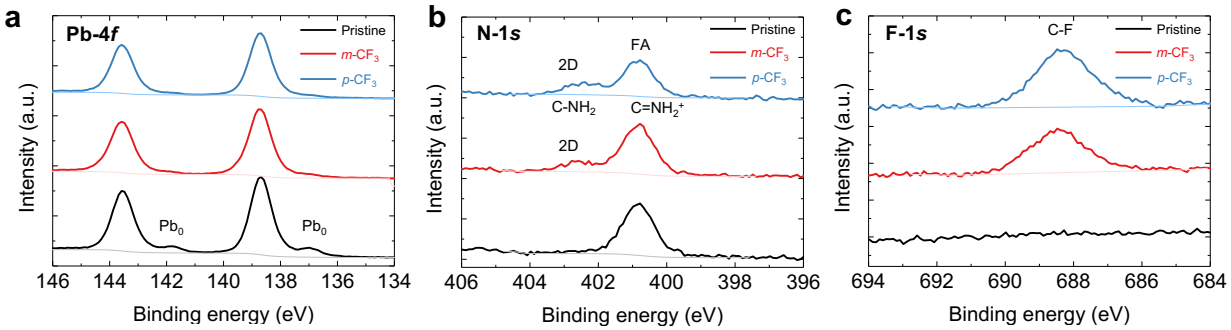

Figure S13. XPS spectra of (a) Pb-4*f* core-level spectra, (b) N-1*s* core-level spectra and F-1*s* core-level spectra in perovskite films treated with different organic iodide salt .

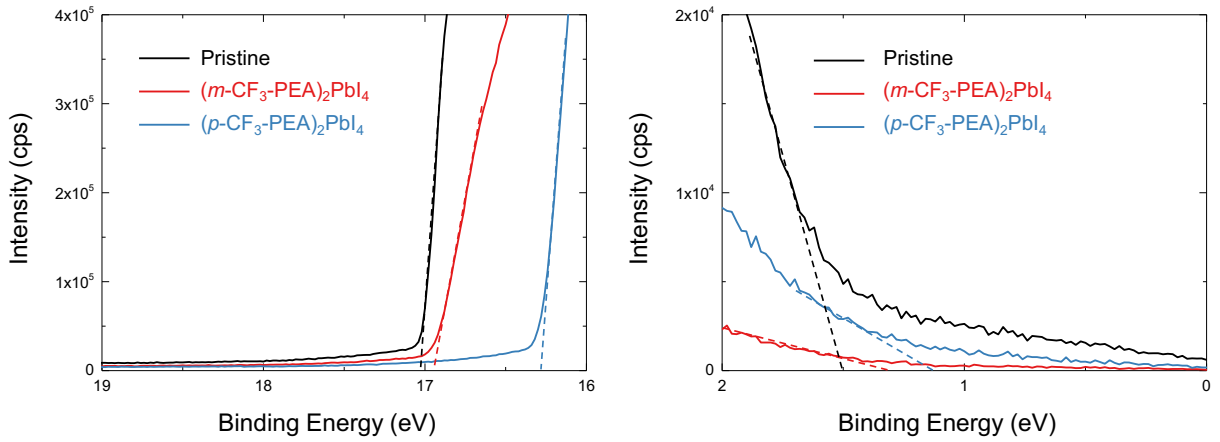

Figure S14. UPS spectra of pristine 3D perovskite, pure (m-CF_3-PEA)$_2$PbI$_4$, and (p-CF_3-PEA)$_2$PbI$_4$ films.

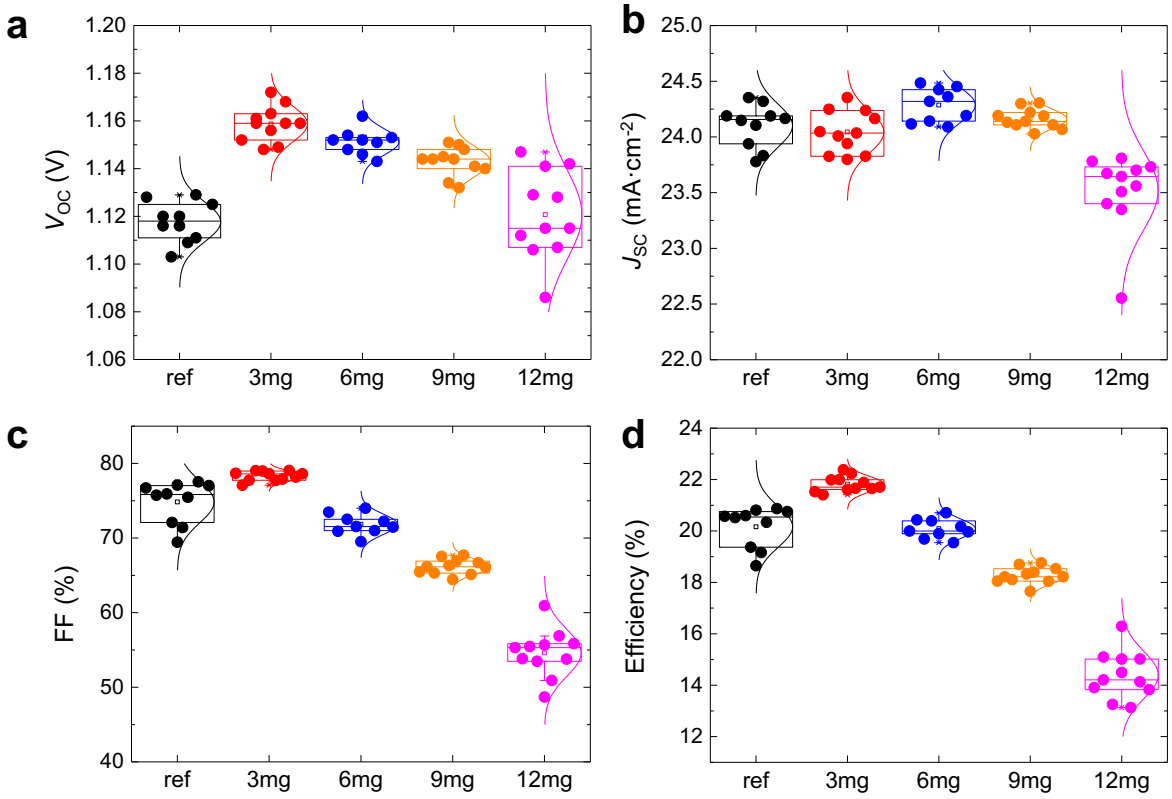

Figure S15. (a) V_{oc}, (b) J_{sc}, (c) FF, and (d) PCE histograms for devices with anti-reflective film attached using perovskite layers by different *m*-CF_3 PEAI concentration in 1 mL IPA solution under 1-Sun illumination.

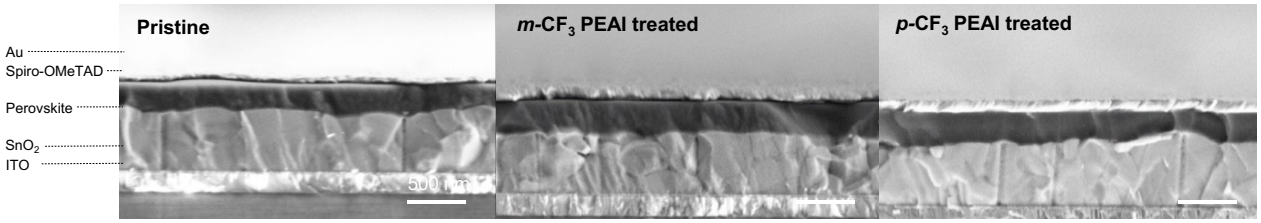

Figure S16. Cross sectional SEM images of the device with pristine 3D perovskite film, *m*-CF_3 PEAI treated-, and *p*-CF_3 PEAI treated 2D/3D perovskite film. All scale bars, 500 nm.

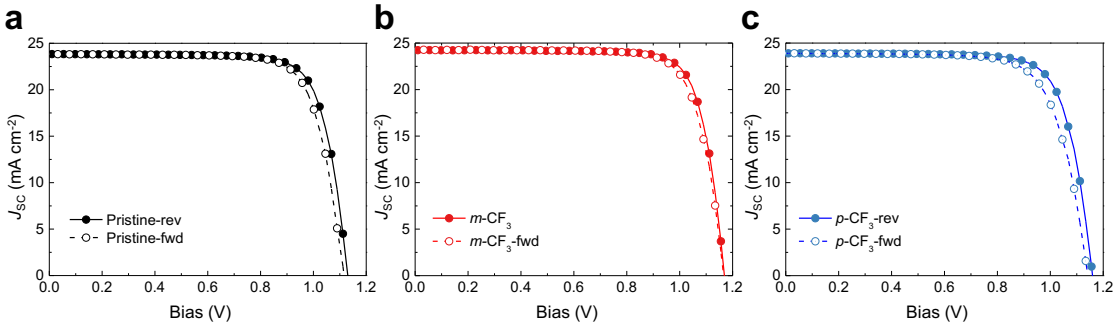

	V_{oc} (V)	J_{sc}(mA/cm^2)	FF (%)	Efficiency (%)
Pristine-rev	1.13	23.8	77.5	20.9
Pristine-fwd	1.12	23.8	76.2	20.3
m-CF_3-rev	1.17	24.2	79.0	22.4
m-CF_3-fwd	1.17	24.3	77.3	21.9
p-CF_3-rev	1.16	23.9	76.7	21.3
p-CF_3-fwd	1.14	23.9	73.5	20.1

Figure S17. *J-V* curves of best performing photovoltaics with (a) pristine 3D perovskite, (b) *m*-CF_3 PEAI treated perovskite, and (c) *p*-CF_3 PEAI treated perovskite at both reverse and forward scan. Solid lines and dashed lines indicate reverse scans and forward scans, respectively.

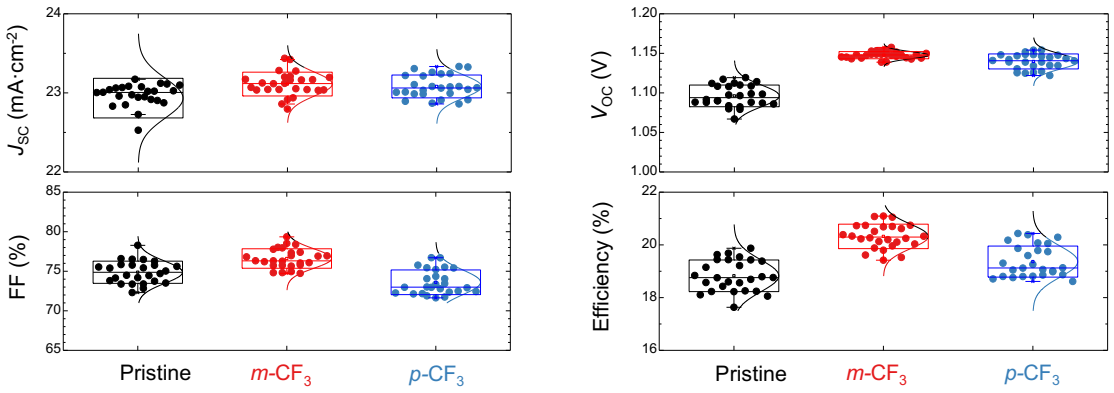

Figure S18. Device performance histograms of perovskite solar cells before anti-reflective films.

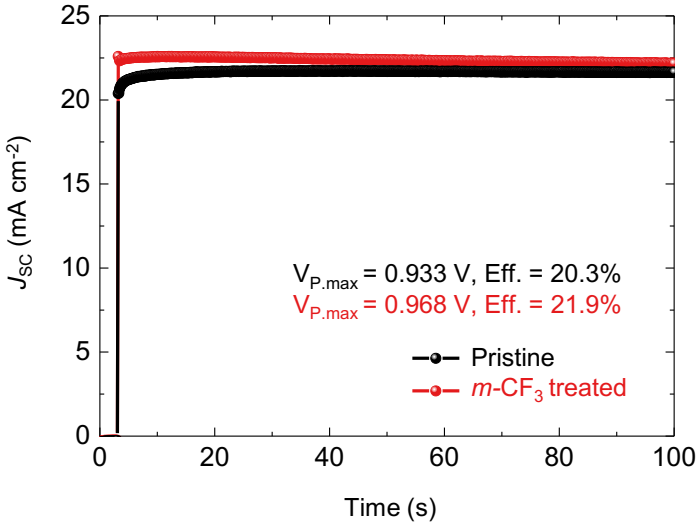

Figure S19. Stabilized power output (SPO) of device with pristine 3D perovskite and *m*-CF_3 PEAI treated perovskite films measured at corresponding maximum power points.

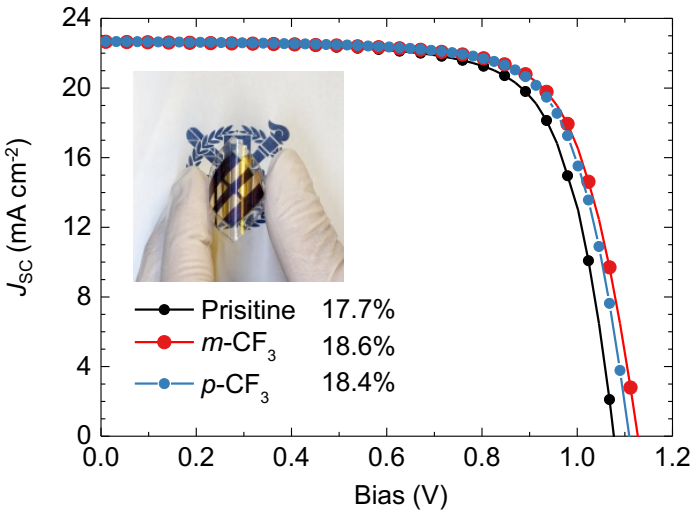

Figure S20. *J-V* curves of flexible device with pristine 3D perovskite, m-CF_3 PEAI treated perovskite, and p-CF_3 PEAI treated perovskite at both reverse and forward scan.

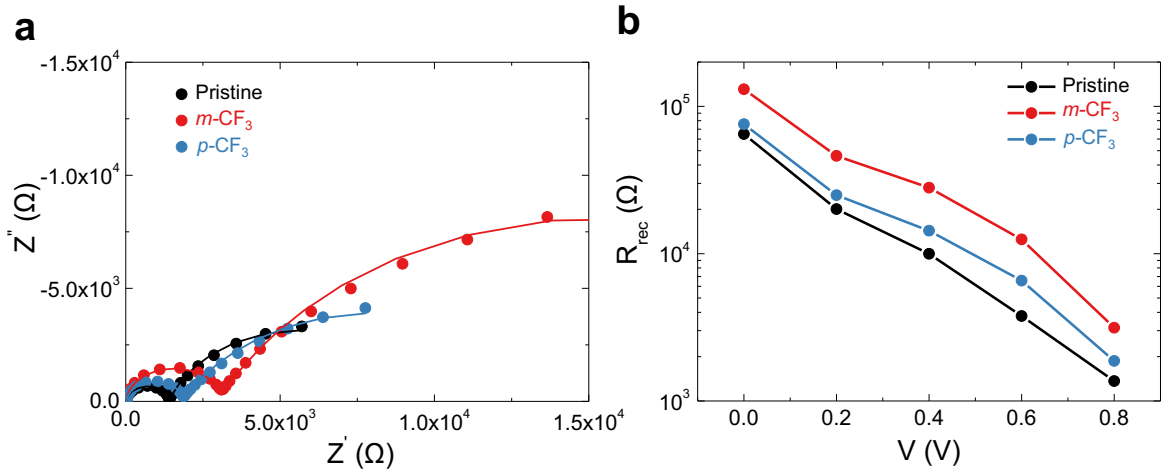

Figure S21. (a) Nyquist plots from EIS measurements with an applied voltage of 0.4 V. (b) Voltage dependent surface recombination resistance ($R_{S.Rec}$) of the devices using pristine perovskite films, *m*-CF_3 PEAI treated- and *p*-CF_3 PEAI treated perovskite films.

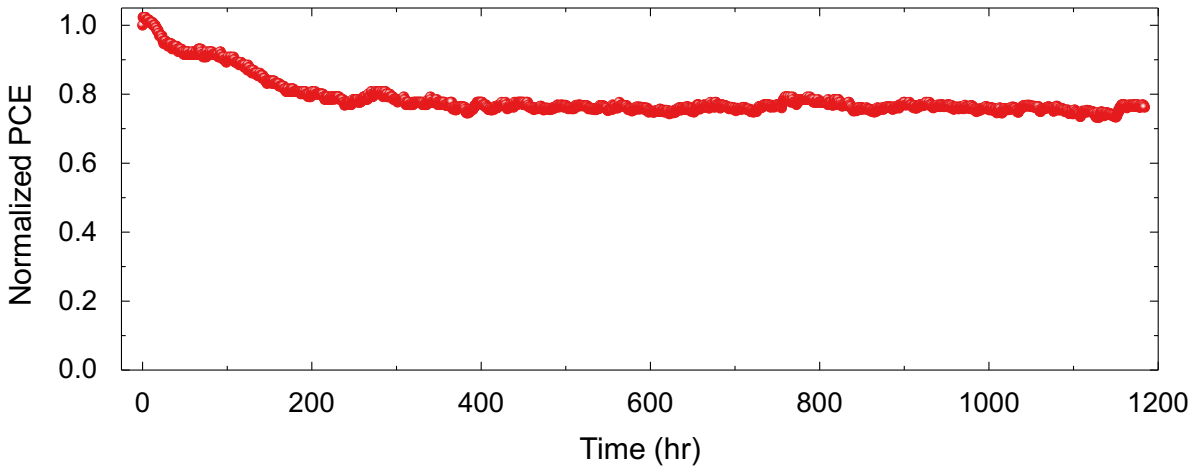

Figure S22. Operational photo-stability of *m*-CF_3 PEAI treated device with encapsulation under 1-Sun illumination.

REFERENCES specific to SI

1. Traoré, B.; Basera, P.; Ramadan, A. J.; Snaith, H. J.; Katan, C.; Even, J., A Theoretical Framework for Microscopic Surface and Interface Dipoles, Work Functions, and Valence Band Alignments in 2D and 3D Halide Perovskite Heterostructures. *ACS Energy Lett*. **2021**, 7 (1), 349-357.

2. Traore, B.; Pedesseau, L.; Assam, L.; Che, X.; Blancon, J. C.; Tsai, H.; Nie, W.; Stoumpos, C. C.; Kanatzidis, M. G.; Tretiak, S.; Mohite, A. D.; Even, J.; Kepenekian, M.; Katan, C., Composite Nature of Layered Hybrid Perovskites: Assessment on Quantum and Dielectric Confinements and Band Alignment. *ACS Nano* **2018**, 12 (4), 3321-3332.